

# Electron-phonon coupling superconductivity in two-dimensional orthorhombic $MB_6$ ( $M = Mg, Ca, Ti, Y$ ) and hexagonal $MB_6$ ( $M = Mg, Ca, Sc, Ti$ )

Tao Bo,<sup>1,2</sup> Peng-Fei Liu,<sup>1</sup> Luo Yan,<sup>1</sup> and Bao-Tian Wang<sup>1,3,\*</sup>

<sup>1</sup>*Spallation Neutron Source Science Center, Institute of High Energy Physics, Chinese Academy of Sciences (CAS), Dongguan, Guangdong 523803, China*

<sup>2</sup>*Songshan Lake Materials Laboratory, Dongguan, Guangdong 523808, China*

<sup>3</sup>*Collaborative Innovation Center of Extreme Optics, Shanxi University, Taiyuan, Shanxi 030006, China*



(Received 18 June 2020; accepted 2 November 2020; published 16 November 2020)

Combining crystal structure search and first-principles calculations, we report a series of two-dimensional (2D) metal borides including orthorhombic (ort-) $MB_6$  ( $M = Mg, Ca, Ti, Y$ ) and hexagonal (hex-) $MB_6$  ( $M = Mg, Ca, Sc, Ti$ ). Then, we investigate their geometrical structures, bonding properties, electronic structures, mechanical properties, phonon dispersions, thermal stability, dynamic stability, charge density wave (CDW) phase transition, electron-phonon coupling (EPC), superconducting properties, and so on. Our *ab initio* molecular dynamics simulation results show that these  $MB_6$  can maintain their original configurations up to about 1000 or 700 K (only for hex- $MgB_6$ ), indicating their excellent thermal stability. All their elastic constants satisfy the Born mechanically stable criteria and no imaginary frequencies are observed in their phonon dispersions. Interestingly, there may exist a CDW phase transition for ort-TiB<sub>6</sub> from type-I to type-II 2 × 1 supercell structure and for ort-YB<sub>6</sub> from type-I to type-III 2 × 1 supercell structure. Besides, these 2D  $MB_6$  are all predicted to be intrinsic phonon-mediated superconductors. By analytically solving the McMillan-Allen-Dynes formula derived from the microscopic theory of Bardeen, Cooper, and Schrieffer, we obtain the superconducting transition temperature ( $T_c$ ) for these materials, which are in the range of 1.4–22.6 K. Among our studied  $MB_6$ , the highest  $T_c$  (22.6 K) appears in hex-CaB<sub>6</sub>, whose EPC constant ( $\lambda$ ) is 0.87. By applying tensile/compressive strains on ort-/hex-CaB<sub>6</sub>, we find that the compressive strain can obviously soften the acoustic-phonon branch and enhance the EPC as well as  $T_c$ . The  $T_c$  of the hex-CaB<sub>6</sub> can be increased from 22.6 to 28.4 K under compressive strain of 3%. These findings enrich the database of 2D superconductors and should stimulate experimental synthesizing and characterizing of 2D superconducting metal borides.

DOI: 10.1103/PhysRevMaterials.4.114802

## I. INTRODUCTION

Superconducting materials have excellent physical and chemical properties, and may be widely used in electric power, electronics, medical, transportation, high-energy physics, and other fields. In addition to the hot topics of copper oxide [1] and iron-based superconductors [2], conventional electron-phonon superconductors are still attractive [3]. Among reported conventional phonon-mediated superconductors, the anisotropic two-gap superconductor MgB<sub>2</sub> ever holds the record of the highest superconducting transition temperature ( $T_c$ ) of 39 K [4]. This discovery has stimulated many efforts in exploring the microscopic mechanisms [5–7] and also in searching for new conventional superconductors [8,9]. The predicted superconductors of hydrogen sulfide [10] and LaH<sub>10</sub> [11], based upon the Bardeen-Cooper-Schrieffer (BCS) theory [12], have been experimentally verified [13–15]. Their  $T_c$  of 203 K at 90 GPa and 250 K at 170 GPa have greatly overcome the  $T_c$  of MgB<sub>2</sub>.

Reducing dimensionality of materials can modulate their properties and would also produce new structures. With

the development of the low-dimensional nanostructure technology, many two-dimensional (2D) superconductors have been successfully synthesized [16,17], such as  $\alpha$ -Mo<sub>2</sub>C [18], Li-decorated monolayer graphene [19], NbSe<sub>2</sub> [20], potassium-intercalated  $T_d$ -WTe<sub>2</sub> [21], stanene [22], and magic twisted graphene [23]. Fascinating phenomena of the Kosterlitz-Thouless-Berezinskii transition, electron quantum confinement effects, and charge density wave (CDW) have been observed in these 2D superconductors. Thus, it is of great interest to find new 2D superconductors and investigate the underlying superconducting mechanism for not only the basic scientific studies but also the application of superconducting electronic devices in high and new technology. Based upon density functional theory (DFT) and using the BCS theory, many potential 2D superconductors have been predicted, such as the borophene [24–27], aluminum-deposited graphene [28], carrier-doped or strained graphene [29,30],  $\beta_0$ -PC [31], MgB<sub>x</sub> [32], Mo<sub>2</sub>B<sub>2</sub> [33], W<sub>2</sub>B<sub>2</sub> [34], and AlB<sub>6</sub> [35]. Interestingly, competition or coexistence of the CDW and superconducting order in 2D TiSe<sub>2</sub> [36] and NbSe<sub>2</sub> [37], hydrogenation superconducting monolayer MgB<sub>2</sub> [38], Na-intercalated superconducting MoX<sub>2</sub> ( $X = S, Se$ ) bilayers [39], Ca-intercalated  $\beta$ -Sb bilayer superconductor [40], electron/hole-doped superconducting PtSe<sub>2</sub> [41], and

\*Corresponding author: wangbt@ihep.ac.cn

Br-functionalized superconducting monolayer Mo<sub>2</sub>C [42] have been studied.

The superconductivity with high  $T_c$  may exist in materials composed of light atoms [43]. Boron has a very small atomic mass, which may enable superconducting behaviors in its elemental or alloying forms. Experimentally, a high  $T_c$  of 36 K was observed in boron-doped  $Q$  carbon [8]. In bulk YB<sub>6</sub>, a  $T_c$  of  $\sim$ 7 K was reported through measuring its specific heat, resistivity, and magnetic susceptibility [44]. Until now, superconducting properties have never been experimentally observed in 2D boron and 2D borides. The difficulty may appear in the synthesizing and also in measuring. However, in recent years, many borophenes and 2D metal borides have been predicted to be superconductors, such as  $\beta_{12}$  borophene [24–26],  $\chi_3$  borophene [25], B<sub>x</sub>MgB<sub>x</sub> ( $x = 2\text{--}5$ ) borides [32], and AlB<sub>6</sub> nanosheet [35]. The  $T_c$  of  $\beta_{12}$  borophene is greatly suppressed by biaxial tensile strain induced by Ag(111) substrate, which explains to some extent the difficulty in experimental measurement [26]. The predicted orthogonal AlB<sub>6</sub> nanosheet not only possesses triple Dirac cones, Dirac-like fermions, and node-loop features, but also has superconductivity with  $T_c = 4.7$  K [35].

Recently, we also predicted some 2D superconductors of Mo<sub>2</sub>B<sub>2</sub> [33], W<sub>2</sub>B<sub>2</sub> [34], and XB<sub>6</sub> ( $X = \text{Ga, In}$ ) [45] based on the crystal structure prediction method and first-principles calculations. A certain tensile/compressive strain can regulate the electron-phonon coupling (EPC) as well as  $T_c$  of these materials. In the present work, we first report a series of 2D MB<sub>6</sub> structures including orthogonal (ort-)MgB<sub>6</sub>, CaB<sub>6</sub>, TiB<sub>6</sub>, YB<sub>6</sub>, and hexagonal (hex-)MgB<sub>6</sub>, CaB<sub>6</sub>, ScB<sub>6</sub>, and TiB<sub>6</sub> through structural searching by using the CALYPSO code. Then, we investigate their crystal structures, electronic structures, phonon dispersions, mechanical properties, CDW phase transition, EPC, and superconducting properties by performing first-principles calculations. Based upon the BCS theory, by analytically solving the McMillan-Allen-Dynes formula, we find that these 2D metal hexaborides are all phonon-mediated superconductors with  $T_c$  in range of 1.4–22.6 K. The underlying mechanism of their superconductivity is carefully analyzed. In addition, the effect of tensile/compressive strain on the EPC constant and superconducting properties is also studied.

## II. COMPUTATIONAL DETAILS

We search for 2D MB<sub>6</sub> ( $M = \text{Mg, Ca, Sc, Ti, Sr, Y}$ ) using the particle swarm optimization (PSO) scheme as implemented in the CALYPSO code [46–48]. In searching, both planar and buckled structures including one, two, and three layers are considered. For each MB<sub>6</sub> system, one, two, and four formula units per simulation cell are calculated. The number of generations is set to be 30 and each generation contains 30 structures. After structural searching, thousands of 2D MB<sub>6</sub> structures are generated. The subsequent structural optimization, energy calculations, and *ab initio* molecular dynamics (AIMD) simulations are carried out by utilizing the density functional theory (DFT) method as implemented in the Vienna Ab initio Simulation Package (VASP) [49]. The Perdew-Burke-Ernzerhof generalized gradient approximation (PBE-GGA) [50] is employed and the electron-ion interaction

is described by using the projector augmented wave (PAW) method [51]. The plane-wave cutoff energy is set as 600 eV and the Brillouin zone (BZ) integration is performed using a  $11 \times 11 \times 1$  Monkhorst-Pack (MP) mesh. All the geometries are relaxed until all forces on the atoms are smaller than 0.005 eV Å<sup>-1</sup>. A vacuum separation is set to more than 20 Å to prevent any interactions between two neighboring monolayers. The AIMD simulations in the *NVT* ensemble are employed at 300, 700, and 1000 K to investigate the thermal stability of these 2D MB<sub>6</sub> monolayers. They are performed by using  $3 \times 3$  supercells with a time step of 1 fs and total simulation of 5 ps.

The calculations of band structure, phonon dispersion, EPC, and superconducting property are performed at the DFT level, employing the norm-conserving pseudopotentials [52] as implemented in the QUANTUM-ESPRESSO (QE) package [53]. The VASP-optimized structures are reoptimized within QE. The plane-wave kinetic-energy cutoff and the energy cutoff for charge density are set as 80 and 320 Ry, respectively. The Methfessel-Paxton smearing width of 0.02 Ry is used. The BZ  $k$ -point grid of  $32 \times 32 \times 1$  is adopted for the self-consistent electron-density calculations. The dynamic matrix and EPC matrix elements are calculated on  $8 \times 8 \times 1$  and  $16 \times 16 \times 1$   $q$ -point meshes for *ort-* and *hex-MB<sub>6</sub>* monolayers, respectively. The convergence test of the  $q$ -point meshes is presented in Fig. S1 and Table S1 in the Supplemental Material (SM) [54]. The phonon properties and EPC are calculated within the density-functional perturbation theory [55] and Eliashberg theory [3].

The EPC  $\lambda_{qv}$  is calculated according to the Migdal-Eliashberg theory [3] by

$$\lambda_{qv} = \frac{\gamma_{qv}}{\pi h N(E_F) \omega_{qv}^2}, \quad (1)$$

where  $\gamma_{qv}$  is the phonon linewidth,  $\omega_{qv}$  is the phonon frequency, and  $N(E_F)$  is the electronic density of state at the Fermi level. The  $\gamma_{qv}$  can be estimated by

$$\gamma_{qv} = \frac{2\pi\omega_{qv}}{\Omega_{BZ}} \sum_{k,n,m} |g_{kn,k+qm}^v|^2 \delta(\epsilon_{kn} - \epsilon_F) \delta(\epsilon_{k+qm} - \epsilon_F), \quad (2)$$

where  $\Omega_{BZ}$  is the volume of the BZ,  $\epsilon_{kn}$  and  $\epsilon_{k+qm}$  indicate the Kohn-Sham energy, and  $g_{kn,k+qm}^v$  represents the EPC matrix element. The Eliashberg spectral function  $\alpha^2 F(\omega)$  can be estimated by

$$\begin{aligned} \alpha^2 F(\omega) &= \frac{1}{2\pi N(E_F)} \sum_{qv} \frac{\gamma_{qv}}{h\omega_{qv}} \delta(\omega - \omega_{qv}) \\ &= \sum_{qv} \frac{\lambda_{qv}\omega_{qv}}{2} \delta(\omega - \omega_{qv}). \end{aligned} \quad (3)$$

Then, the EPC constant  $\lambda(\omega)$  and the logarithmic average frequency  $\omega_{\ln}(\omega)$  can be determined by

$$\lambda(\omega) = 2 \int_0^\omega \frac{\alpha^2 F(\omega)}{\omega} d\omega \quad (4)$$

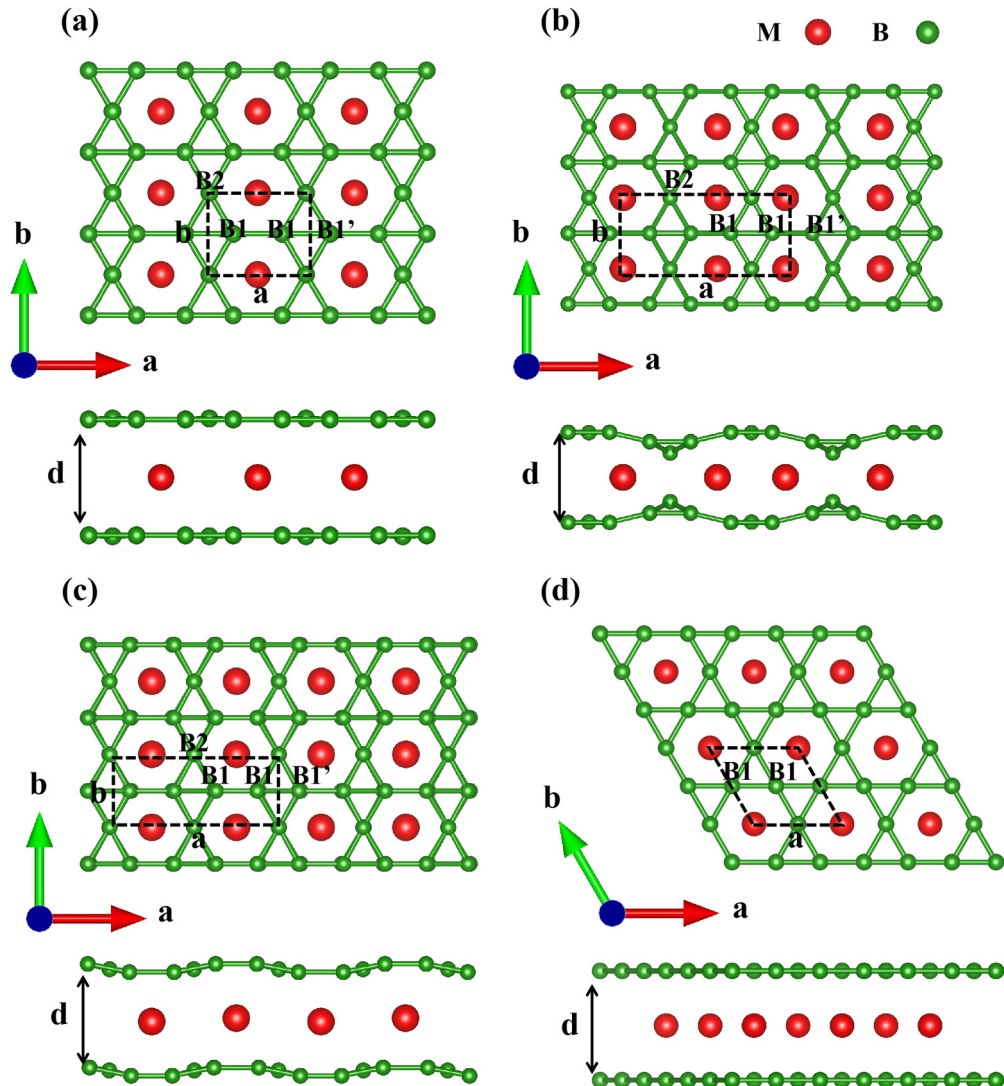


FIG. 1. Top and side views of the (a) type-I ort- $MB_6$  ( $M = Mg, Ca, Sc, Sr$ ), (b) type-II ort- $TiB_6$ , (c) type-III ort- $YB_6$ , and (d) hex- $MB_6$  ( $M = Mg, Ca, Sc, Ti, Sr, Y$ ) monolayers.

and

$$\omega_{ln}(\omega) = \exp \left[ \frac{2}{\lambda} \int_0^{\infty} \frac{d\omega}{\omega} \alpha^2 F(\omega) \ln \omega \right]. \quad (5)$$

After obtaining the total  $\lambda$  and  $\omega_{ln}$ , the superconducting transition temperature  $T_c$  can be calculated by the McMillan equation [56], further modified by Allen and Dynes [57,58],

$$T_c = \frac{\omega_{ln}}{1.2} \exp \left[ -\frac{1.04(1+\lambda)}{\lambda - \mu^*(1+0.62\lambda)} \right]. \quad (6)$$

Here,  $\mu^*$  is an empirical parameter that describes the effective screened Coulomb repulsion. The detailed description of  $\mu^*$  is in the SM [54,59]. Actually, it is hard to determine this parameter within the present computational scheme [24].  $\mu^*$  has typical values between 0.1 and 0.15 [25]. For 2D borophenes,  $\mu^* = 0.1$  was used in much of the literature to calculate the superconductivity [24,25,60,61]. In our following calculations, in order to compare with the results of borophenes,

the same value  $\mu^* = 0.1$  is used. In addition, we also present the variation of  $T_c$  with  $\mu^*$  ( $0.5 \leq \mu^* \leq 1.5$ ) for our studied  $MB_6$  materials.

### III. RESULTS AND DISCUSSION

#### A. Geometrical structures and bonding nature of the ort- and hex- $MB_6$

We perform a comprehensive structural search using the CALYPSO code to find various configurations of 2D  $MB_6$ . After more calculations and analysis for the structures, we obtain the global minimum structures for 2D  $MB_6$  ( $M = Mg, Ca, Sc, Sr$ ) [see Fig. 1(a), type-I orthogonal configuration], 2D  $TiB_6$  [see Fig. 1(b), type-II orthogonal configuration], and 2D  $YB_6$  [see Fig. 1(c), type-III orthogonal configuration]. The energies of these global minimum  $MB_6$  in sequence of  $M = Mg, Ca, Sc, Ti, Sr, Y$  are 1.038, 0.888, 0.100, 0.256, 0.961, and 0.155 eV per formula unit lower than those of

TABLE I. Lattice parameters ( $\text{\AA}$ ), bond lengths ( $\text{\AA}$ ), and cohesive energies (eV) of  $MB_6$ .

	<i>a</i>	<i>b</i>	<i>d</i>	B1-B1/B1-B1'	B1-B2	M-B1	M-B2	<i>M-M</i>	Cohesive energy
Type-I ort-MgB <sub>6</sub>	3.46	2.90	3.55	1.73/1.73	1.70	2.50	2.48	2.90/3.46	5.66
Type-I ort-CaB <sub>6</sub>	3.49	2.94	4.24	1.76/1.72	1.70	2.70	2.74	2.94/3.49	5.75
Type-II ort-TiB <sub>6</sub>	6.76	2.95	3.73	1.71/1.72	1.77	2.37/2.46	2.21/2.34	2.84/2.95	6.59
Type-III ort-YB <sub>6</sub>	6.88	2.97	4.22	1.68/1.72	1.75	2.66/2.79	2.63/2.73	2.97/3.45	6.18
hex-MgB <sub>6</sub>	3.41		3.63	1.70		2.49		3.41	5.52
hex-CaB <sub>6</sub>	3.43		4.26	1.71		2.73		3.43	5.62
hex-ScB <sub>6</sub>	3.41		3.73	1.70		2.53		3.41	6.26
hex-TiB <sub>6</sub>	3.41		3.33	1.70		2.38		3.41	6.56

their corresponding hexagonal phase, respectively. In one recent theoretical work [32], the energy of type-I ort-MgB<sub>6</sub> was also reported lower by 1.02 eV per unit cell than that of the hex-MgB<sub>6</sub>. The global minimum structure of the 2D AlB<sub>6</sub> [35] is the type-I orthogonal one. However, the phonon spectra results calculated by QE show that type-I ort-ScB<sub>6</sub>, type-I ort-SrB<sub>6</sub>, hex-SrB<sub>6</sub>, and hex-YB<sub>6</sub> are dynamically unstable. Their phonon dispersions are shown in Fig. S2 in the SM [54]. As known, the global minimum energy is not the exclusive condition for experimental synthesis of materials. Under suitable conditions, it is possible to synthesize some metastable crystals with higher energy [62]. On the basis of the aforementioned discussions, in the following, we will focus on the (meta)stable structures including type-I orthogonal  $MB_6$  ( $M = \text{Mg, Ca}$ ), type-II ort-TiB<sub>6</sub>, type-III ort-YB<sub>6</sub>, and hexagonal  $MB_6$  ( $M = \text{Mg, Ca, Sc, Ti}$ ) for further analysis.

The ort- $MB_6$  [see Figs. 1(a)–1(c)] and hex- $MB_6$  [see Fig. 1(d)], consisting of one layer of metal atoms and two layers of B atoms, belong to the orthogonal *Pmmm* (no. 47) and the hexagonal *P6/mmm* (no. 191) space group, respectively. For type-I ort- $MB_6$  [see Fig. 1(a)] and hex- $MB_6$  [see Fig. 1(d)], their B layers are borophenes with hexagonal vacancy density ( $\eta$ ) of 1/4, named  $\delta_4$  [63], and kagome [64], respectively. The metal atoms, which keep the two B layers from fusing together, are sandwiched by top and bottom B layers. Meanwhile, the metal atoms are anchored and stabilized by the two B layers, leading to the high stability of these 2D materials. As shown in Table I, the optimized lattice parameters are  $a = 3.46$ ,  $b = 2.90 \text{ \AA}$  for type-I ort-MgB<sub>6</sub> and  $a = 3.49$ ,  $b = 2.94 \text{ \AA}$  for type-I ort-CaB<sub>6</sub>, which are comparable to those of AlB<sub>6</sub> ( $a = 3.41$ ,  $b = 2.91 \text{ \AA}$ ) [35]. However, the thickness of type-I ort-CaB<sub>6</sub> (4.24  $\text{\AA}$ ) is much larger than that of type-I ort-MgB<sub>6</sub> (3.55  $\text{\AA}$ ). The same phenomenon also occurs in the hex- $MB_6$ . The lattice constants of these hexagonal structures vary slightly, ranging from  $a = b = 3.41$  to 3.43  $\text{\AA}$ , while the thicknesses vary considerably, ranging from 3.33 to 4.26  $\text{\AA}$ . The lattice constant  $a$  of the hex-MgB<sub>6</sub> (3.41  $\text{\AA}$ ) in our work is almost the same as that of Xie *et al.*'s work [64]. The type-II ort-TiB<sub>6</sub> [see Fig. 1(b)] and type-III ort-YB<sub>6</sub> [see Fig. 1(c)] are actually twice that of the type-I orthogonal configuration in the direction of the  $a$  axis, accompanied by the B layers buckled. Compared with the pristine type-I structure, the metal atoms of the type-II structure move a little to the boundary along the  $a$  direction and the alternative line of the B atoms bends to the interstitial sites separated by the metal atoms. As for the type-III structure, half the atoms move up along the  $z$  direc-

tion and half of the atoms go down, like waves. There is a large imaginary frequency in the phonon dispersions of type-I ort-TiB<sub>6</sub> and -YB<sub>6</sub> (see Fig. S2 [54]), indicating they are dynamically unstable. When the unit cells of type-I ort-TiB<sub>6</sub> and -YB<sub>6</sub> are expanded along  $a$  axis, the energy per formula unit decreases and the imaginary frequency of the phonon dispersions disappears. This indicates that a charge density wave (CDW) phase transition exists for ort-TiB<sub>6</sub> and ort-YB<sub>6</sub>. The optimized lattice parameters are  $a = 6.76$ ,  $b = 2.95 \text{ \AA}$  for type-II ort-TiB<sub>6</sub> and  $a = 6.88$ ,  $b = 2.97 \text{ \AA}$  for type-III ort-YB<sub>6</sub>.

For type-I ort- $MB_6$ , there are two symmetrically distinct atom types for B [see Fig. 1(a), labeled B1 and B2]. As shown in Table I, the Mg-B1/Ca-B1 and Mg-B2/Ca-B2 distances are 2.50/2.70 and 2.48/2.74  $\text{\AA}$ , respectively, which are a little larger than those of type-I AlB<sub>6</sub> (2.409 and 2.262  $\text{\AA}$ , respectively) [35]. The B1-B2 bond length of the ort-MgB<sub>6</sub>/CaB<sub>6</sub> is 1.70  $\text{\AA}$ , almost the same as that of AlB<sub>6</sub> (1.708  $\text{\AA}$ ). There are two types of B1-B1 bonds in ort- $MB_6$ : the bond along one side of the hexagonal holes (B1-B1) and the bond along the diagonal of the rhombus (B1-B1'). The B1-B1 and B1-B1' distances for type-I ort-MgB<sub>6</sub>/CaB<sub>6</sub> are 1.73/1.76 and 1.73/1.72  $\text{\AA}$ , respectively, close to those of AlB<sub>6</sub> (1.688 and 1.723  $\text{\AA}$ , respectively). For type-II ort-TiB<sub>6</sub> and type-III ort-YB<sub>6</sub>, the B-B distances range from 1.68 to 1.77  $\text{\AA}$ , while the M-B distances range from 2.21 to 2.79  $\text{\AA}$ . For the hex- $MB_6$ , there is just one symmetrically distinct atom type for B [see Fig. 1(d), labeled B1]. The B1-B1 distances for these six hex- $MB_6$  monolayers are almost the same, in the range of 1.70–1.71  $\text{\AA}$ . However, the M-B1 distances vary considerably, ranging from 2.38 to 2.73  $\text{\AA}$ . The lattice parameters and bond lengths of the dynamically unstable structures are also shown in Table S2 [54].

To get more information about the bonding, we calculate the line charge density distribution along the nearest B-B and M-B bonds and perform the electron localization function (ELF) [65] and Bader charge analysis [66]. The ELF (see Figs. S3 and S4) pictures as well as the values of Bader charge ( $Q_B$ ) and charge density at the corresponding bond point ( $CD_b$ ) (Table S3) are presented in the SM [54]. For type-I ort-MgB<sub>6</sub>, hex-MgB<sub>6</sub>, hex-ScB<sub>6</sub>, hex-TiB<sub>6</sub>, and type-II ort-TiB<sub>6</sub>, there are mainly covalent bonds between B atoms and ionic bonds between metal atoms and the neighboring B atoms. However, for type-I ort-CaB<sub>6</sub>, hex-CaB<sub>6</sub>, and type-III ort-YB<sub>6</sub>, in addition to the above chemical bonds, there are also metallic bonds between  $M$  atoms. One can see the detailed discussions in the SM [54].

TABLE II. Calculated elastic constants  $C_{ij}$  ( $\text{N m}^{-1}$ ), Young's moduli ( $\text{N m}^{-1}$ ), and Poisson's ratio of  $MB_6$  monolayers.

	$C_{11}$	$C_{22}$	$C_{12}$	$C_{66}$	$Y_x$	$Y_y$	$v_x$	$v_y$
Type-I ort-MgB <sub>6</sub>	361.1	404.8	34.0	110.1	358.2	401.6	0.084	0.094
Type-I ort-CaB <sub>6</sub>	321.2	395.6	23.8	129.3	319.8	393.8	0.060	0.074
Type-II ort-TiB <sub>6</sub>	1244.2	1412.4	28.6	303.8	1243.6	1411.7	0.020	0.023
Type-III ort-YB <sub>6</sub>	1052.6	1627.4	17.8	314.2	1052.4	1627.1	0.011	0.017
hex-MgB <sub>6</sub>	344.7		67.9	145.8	331.3	331.3	0.197	0.197
hex-CaB <sub>6</sub>	340.1		66.0	140.3	327.3	327.3	0.194	0.194
hex-ScB <sub>6</sub>	357.5		68.1	142.7	344.5	344.5	0.190	0.190
hex-TiB <sub>6</sub>	315.5		93.3	107.5	287.9	287.9	0.296	0.296

### B. Stability and mechanical properties of ort- and hex- $MB_6$

It is important to verify the stability of these  $MB_6$  monolayers, which is helpful for judging whether they can be synthesized experimentally. Cohesive energy is a widely accepted parameter used to evaluate the stability of materials. We calculate the cohesive energy  $E_{coh}$  using the following formulas:

$$E_{coh} = \frac{E_M + 6E_B - E_{MB_6}}{7}, \quad (7)$$

where  $E_M$  and  $E_B$  are the total energies of the isolated metal and B atoms, respectively,  $E_{MB_6}$  is the total energy of the 2D  $MB_6$ . As shown in Table I, the calculated cohesive energies are 5.66, 5.75, 6.59, 6.18, 5.52, 5.62, 6.26, and 6.56 eV/atom for type-I ort-MgB<sub>6</sub>, type-I ort-CaB<sub>6</sub>, type-II ort-TiB<sub>6</sub>, type-III ort-YB<sub>6</sub>, hex-MgB<sub>6</sub>, hex-CaB<sub>6</sub>, hex-ScB<sub>6</sub>, and hex-TiB<sub>6</sub>, respectively. The relatively large cohesive energies demonstrate the high stability of these  $MB_6$  monolayers, which is a necessary condition for experimental synthesis. The cohesive energies of these  $MB_6$  are larger than those of the previously computationally predicted and later experimentally fabricated 2D materials, such as Cu<sub>2</sub>Si (3.46 eV/atom) [67,68], Ni<sub>2</sub>Si (4.80 eV/atom) [69], and Cu<sub>2</sub>Ge (3.17 eV/atom) [70]. This indicates that it is possible to synthesize our predicted  $MB_6$  under appropriate experimental conditions. We also calculate the phonon dispersions along the high-symmetry lines as well as the phonon density of states (PhDOS) to evaluate the dynamic stability of these  $MB_6$  monolayers. No imaginary modes in the BZ confirms the lattice dynamic stability of these eight  $MB_6$  monolayers. A detailed discussion of the phonon dispersions will be supplied later. In addition, thermal stability is very important for the practical application of these 2D  $MB_6$  in nanoelectronic devices or electrode films. In order to investigate the thermal stability of these 2D  $MB_6$ , AIMD simulations are performed with total simulation time of 5 ps at 300, 700, and 1000 K. We present in Figs. S5–S7 [54] the variation of total energies with time for the  $MB_6$  monolayers. The snapshots after 5 ps for these simulated  $MB_6$  are shown in Figs. S8–S10 [54]. We find that the total energy of each  $MB_6$  monolayer fluctuates around a constant temperature value up to 1000 or 700 K (only for hex-MgB<sub>6</sub>). After simulating for 5 ps, the hex-MgB<sub>6</sub> monolayer well maintains its original configuration at up to 700 K, while the other  $MB_6$  monolayers maintains at up to 1000 K. The above results indicate the excellent thermal stability of these  $MB_6$  monolayers.

Mechanical properties are also very important for the practical application of 2D materials. In order to accurately

understand the mechanical properties of these  $MB_6$  monolayers, we calculate their elastic constants [71]. Generally speaking, a mechanically stable 2D material needs to satisfy the Born criteria [72],  $C_{11}C_{22} - C_{12}^2 > 0$  and  $C_{66} > 0$ . For hexagonal symmetry,  $C_{11} = C_{22}$ . Thus, the stability criteria are  $|C_{11}| > |C_{12}|$  and  $C_{66} > 0$ . The calculated elastic constants of these eight  $MB_6$  monolayers are listed in Table II. We find that the elastic constants of these  $MB_6$  monolayers all meet the Born criteria, indicating that they are mechanically stable. Based on the elastic constants, the Young's moduli along the  $x$  and  $y$  directions of these materials are calculated according to  $Y_x = \frac{(C_{11}C_{22} - C_{12}C_{21})}{C_{22}}$  and  $Y_y = \frac{(C_{11}C_{22} - C_{12}C_{21})}{C_{11}}$ . For type-I ort-MgB<sub>6</sub>, the values of  $Y_x$  and  $Y_y$  are a little larger than that of the graphene (340 N/m) [73], while for type-I ort-CaB<sub>6</sub>, the  $Y_x$  is a little smaller and the  $Y_y$  is a little larger than that of the graphene (340 N/m), which indicates that these two monolayers have excellent mechanical properties along both the  $x$  and  $y$  directions. For type-II ort-TiB<sub>6</sub> and type-III ort-YB<sub>6</sub>, the values of  $Y_x$  and  $Y_y$  are much larger than that of the graphene (340 N/m), indicating the remarkable mechanical properties for them. For the hex-MgB<sub>6</sub>, hex-CaB<sub>6</sub>, and hex-ScB<sub>6</sub>, the values of  $Y_x/Y_y$  differ a little from that of the graphene (340 N/m), also exhibiting excellent mechanical properties. However, for the hex-TiB<sub>6</sub>, the values of  $Y_x/Y_y$  are smaller than those of the other hexagonal  $MB_6$ , indicating relatively weak mechanical properties. We also calculate the Poisson's ratio by  $v_x = \frac{C_{21}}{C_{22}}$  and  $v_y = \frac{C_{12}}{C_{11}}$  based on the calculated elastic constants. For type-I ort-MgB<sub>6</sub> and ort-CaB<sub>6</sub>, type-II ort-TiB<sub>6</sub>, and type-III ort-YB<sub>6</sub>, the  $v_x$  and  $v_y$  values (0.011–0.094) are much smaller than that of the graphene ( $v = 0.173$ ) [74], indicating that the compression in the  $y/x$  direction is very small when stretching in the  $x/y$  direction. For the hexagonal  $MB_6$  monolayers except hex-TiB<sub>6</sub>, the  $v_x/v_y$  values (0.190–0.197) are similar to that of graphene ( $v = 0.173$ ). However, for the hex-TiB<sub>6</sub>, the  $v_x/v_y$  values ( $v = 0.296$ ) are much larger than that of graphene ( $v = 0.173$ ), indicating large compression in the  $y/x$  direction when stretching in the  $x/y$  direction.

### C. Electronic properties

For all these  $MB_6$  monolayers, we show the orbital-resolved band structures and electronic density of states (DOS) in Fig. 2. The corresponding Fermi surfaces (FSs) are shown in Fig. 3. We find that all these materials exhibit metallic properties because there are many bands crossing the Fermi energy level. For type-I ort-MgB<sub>6</sub>, type-I ort-CaB<sub>6</sub>,

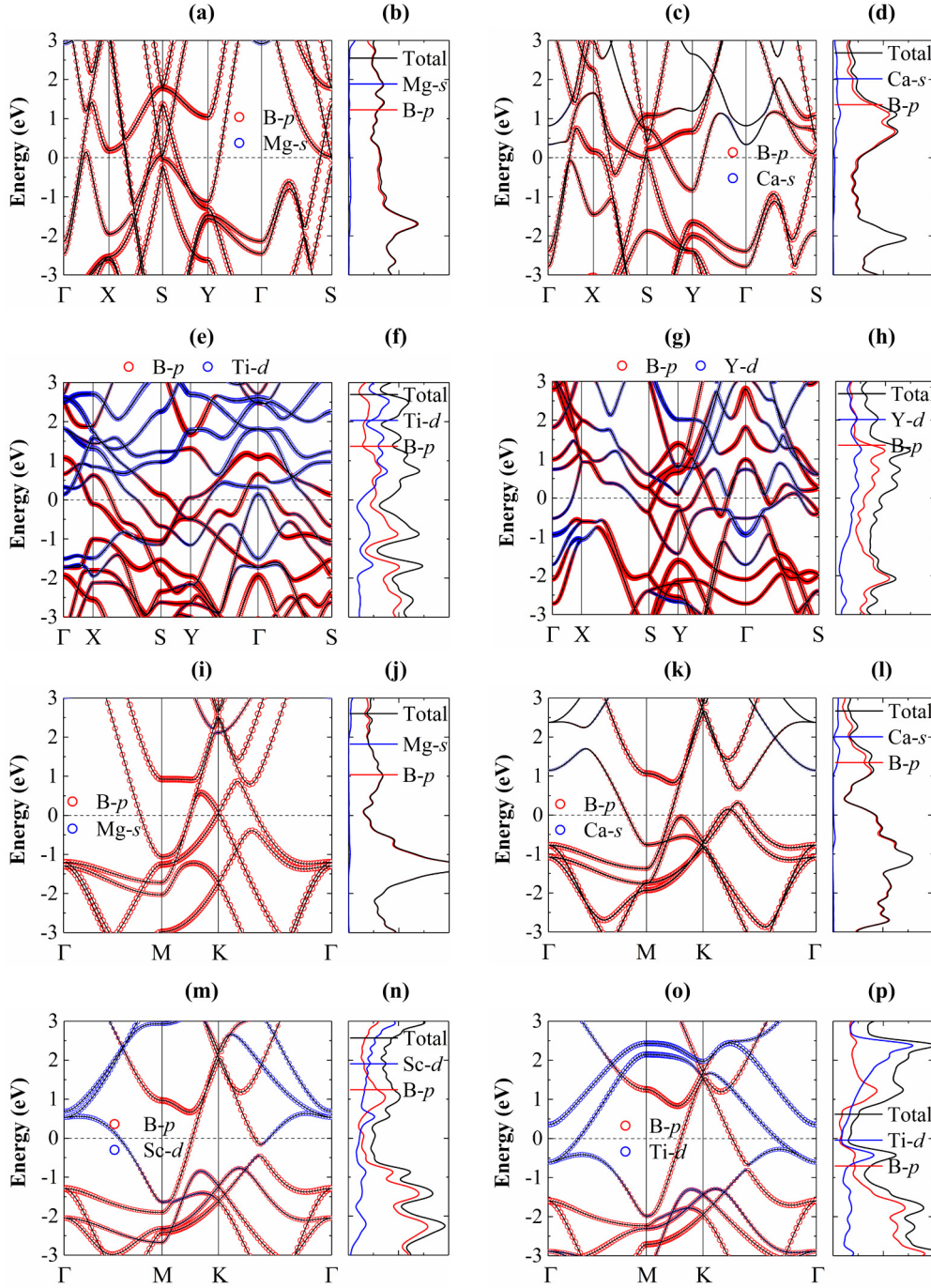


FIG. 2. Orbital-resolved band structures and corresponding total and local DOSs of (a),(b) type-I ort-MgB<sub>6</sub>, (c),(d) type-I ort-CaB<sub>6</sub>, (e),(f) type-II ort-TiB<sub>6</sub>, (g),(h) type-III ort-YB<sub>6</sub>, (i),(j) hex-MgB<sub>6</sub>, (k),(l) hex-CaB<sub>6</sub>, (m),(n) hex-ScB<sub>6</sub>, and (o),(p) hex-TiB<sub>6</sub>.

hex-MgB<sub>6</sub>, and hex-CaB<sub>6</sub>, the B 2p orbitals dominate the bands around the Fermi level, while the metal atomic orbitals have almost no component at the Fermi level. However, for type-II ort-TiB<sub>6</sub>, type-III ort-YB<sub>6</sub>, hex-ScB<sub>6</sub>, and hex-TiB<sub>6</sub>, both B 2p and M d orbitals ( $M = \text{Sc}, \text{Ti}, \text{Y}$ ) dominate the bands around the Fermi level. For type-I ort-MgB<sub>6</sub>, there are several Dirac cones above the Fermi level, close to the high-symmetry point S in the first BZ, which is similar to that of type-I ort-AlB<sub>6</sub> [35]. There are many bands crossing the Fermi level, which forms five pockets at the FS. As shown in Fig. 3(a), there are two pockets centered at the X and Y

points, respectively, one pocket along the  $\Gamma$ -X line, and two pockets along the X-S line. For type-I ort-CaB<sub>6</sub>, there are one, three, one, and one band(s) crossing the Fermi level along  $\Gamma$ -X, X-S, S-Y, and Y- $\Gamma$ , respectively. As shown in Fig. 3(b), these bands form one dumbbell-shaped pocket centered on X, one elliptical pocket centered on Y, and one pocket along X-S. For type-II ort-TiB<sub>6</sub>, there are one, two, two, three, and three band(s) crossing the Fermi level along  $\Gamma$ -X, X-S, S-Y, Y- $\Gamma$ , and  $\Gamma$ -S, respectively. As shown in Fig. 3(c), there is one dumbbell-shaped pocket centered at  $\Gamma$  and one elliptical pocket along S-Y. For type-III ort-YB<sub>6</sub>, there are also many

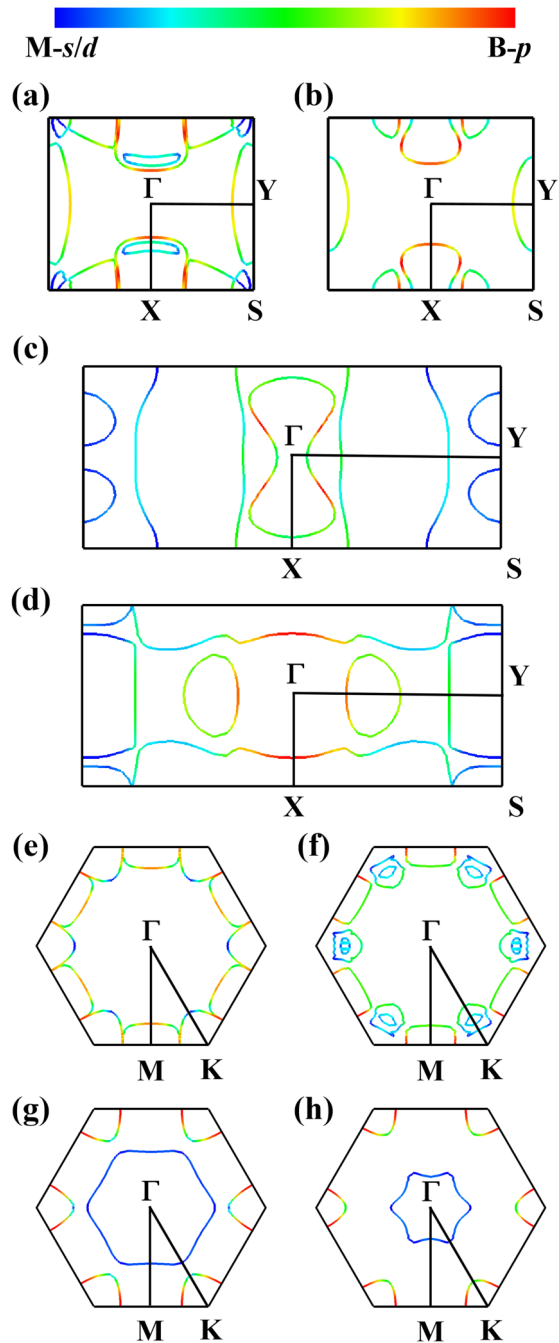


FIG. 3. Fermi surfaces of (a) type-I ort-MgB<sub>6</sub>, (b) type-I ort-CaB<sub>6</sub>, (c) type-II ort-TiB<sub>6</sub>, (d) type-III ort-YB<sub>6</sub>, (e) hex-MgB<sub>6</sub>, (f) hex-CaB<sub>6</sub>, (g) hex-ScB<sub>6</sub>, and (h) hex-TiB<sub>6</sub>.

bands crossing the Fermi level, forming four pockets at the FS. As shown in Fig. 3(d), there are three pockets centered at X, S, and Y, respectively, and one pocket along the  $\Gamma$ -Y line. For hex-MgB<sub>6</sub>, at the K point, there is one Dirac cone across the Fermi level whose states are mainly from the 2p orbitals of the B kagome lattice. This phenomenon has also been observed in one recent theoretical work [64]. Actually, kagome 2D lattice has been extensively studied owing to its unique physics related to Dirac bands [75]. There are one, two, and one band(s) crossing the Fermi level along  $\Gamma$ -M, M-K, and K- $\Gamma$ , respectively, which form a rectangular pocket

centered on M and an elliptical pocket centered on K at the FS [see Fig. 3(e)]. For hex-CaB<sub>6</sub>, there are one, one, and four bands crossing the Fermi level along  $\Gamma$ -M, M-K, and K- $\Gamma$ , respectively. As shown in Fig. 3(f), there is one rectangular pocket centered on M and two pockets along K- $\Gamma$  at the FS of hex-CaB<sub>6</sub>. For hex-ScB<sub>6</sub> and hex-TiB<sub>6</sub>, there are one, one, and two band(s) crossing the Fermi level along  $\Gamma$ -M, M-K, and K- $\Gamma$ , respectively, which are mainly dominated by B 2p and Sc-3d/Ti-3d orbitals. As shown in Figs. 3(g) and 3(h), the FSs of these two materials all include one hexagonal star-shaped pocket centered on  $\Gamma$  and an elliptical pocket centered on K. The hexagonal star-shaped pocket of hex-ScB<sub>6</sub> is larger than that of hex-TiB<sub>6</sub>. From our calculated electronic DOSs, the amplitudes of the  $N(E_F)$  for hex-CaB<sub>6</sub>, type-II ort-TiB<sub>6</sub>, and type-III ort-YB<sub>6</sub> are relatively larger than those of the other MB<sub>6</sub>, which promotes the superconductivity of these three 2D materials.

#### D. EPC and superconductivity

In order to investigate the EPC and superconducting transition temperature  $T_c$  of these 2D MB<sub>6</sub>, we calculate their phonon dispersions, PhDOS, Eliashberg spectral function  $\alpha^2 F(\omega)$ , and  $\lambda(\omega)$  and present them in Figs. 4–6. No imaginary phonon modes in the phonon dispersions clearly indicates that these materials are dynamically stable. The EPC integrated over all phonon branches and distributed in the BZ are shown in Fig. 7 for these eight materials. Our calculated phonon spectra for type-I ort-MgB<sub>6</sub> are consistent with those presented in Liao's work [32]. From our decomposed phonon dispersions, we find that the Mg vibrations and the out-of-plane B<sub>z</sub> vibrations dominate the low frequencies below 500 cm<sup>-1</sup>, while the in-plane B<sub>xy</sub> vibrations dominate the high frequencies above 500 cm<sup>-1</sup>. The low-frequency phonons (100–300 cm<sup>-1</sup>) around the X point, mainly associated with the B<sub>z</sub> vibrations, contribute 68% of the total EPC ( $\lambda = 0.59$ ). As shown in Fig. 7(a), the region around the X point possesses the largest EPC, which is consistent with the EPC  $\lambda_{qv}$  in Fig. 4(b). The phonons (300–400 cm<sup>-1</sup>) along the S-Y- $\Gamma$ -S line, also mainly associated with the B<sub>z</sub> vibrations, contribute 21% of the total EPC ( $\lambda = 0.59$ ). Finally, we obtain the  $T_c = 9.9$  K for the ort-MgB<sub>6</sub> with  $\omega_{ln} = 447.2$  K. Our calculated  $\lambda = 0.59$ ,  $\omega_{ln} = 447.2$  K, and  $T_c = 9.9$  K of the ort-MgB<sub>6</sub> are comparable to those of Liao's work ( $\lambda = 0.49$ ,  $\omega_{ln} = 554.2$  K, and  $T_c = 6.0$  K) [32]. For type-I ort-CaB<sub>6</sub>, the Ca vibrations mainly dominate the low frequencies of 0–200 cm<sup>-1</sup>, while the B vibrations spread in whole area of the BZ. Surprisingly, there is a softened phonon mode around the Y point, associated with the Ca<sub>xy</sub> vibration, contributing 14% of the total EPC ( $\lambda = 0.57$ ). The phonons (100–400 cm<sup>-1</sup>) in the full BZ, mainly associated with the B<sub>z</sub> vibration, contribute 56% of the total EPC ( $\lambda = 0.57$ ). As shown in Fig. 7(b), the largest EPC appears at the Y point and the EPC spreads in the full BZ. The calculated  $T_c$  is 6.7 K, which is comparable to that of type-I ort-MgB<sub>6</sub>. The EPC values of 0.59 and 0.57 indicate that both type-I ort-MgB<sub>6</sub> and -CaB<sub>6</sub> belong to weak-coupling conventional superconductors.

As mentioned above, type-II ort-TiB<sub>6</sub> and type-III ort-YB<sub>6</sub> are actually supercells of type-I ort-TiB<sub>6</sub> and -YB<sub>6</sub>, respectively. There is imaginary frequency in the phonon dispersions

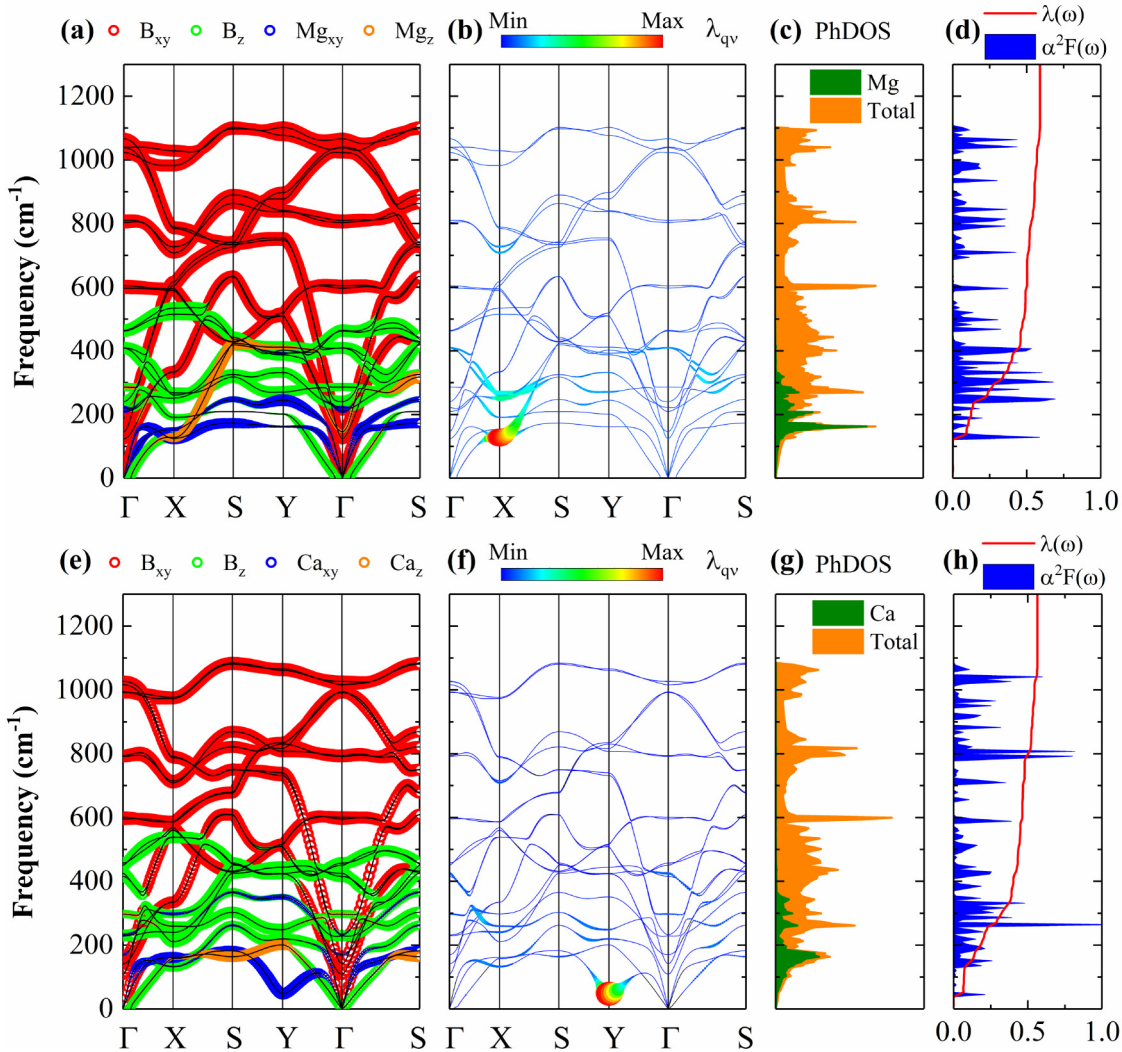


FIG. 4. Phonon dispersions weighted by the motion modes of B, M ( $M = \text{Mg, Ca}$ ) atoms of (a) type-I ort-MgB<sub>6</sub> and (e) type-I ort-CaB<sub>6</sub>. The red, green, blue, and orange hollow circles in (a) and (e) represent B horizontal, B vertical,  $M$  ( $M = \text{Mg, Ca}$ ) horizontal, and  $M$  ( $M = \text{Mg, Ca}$ ) vertical modes, respectively. Phonon dispersions weighted by the magnitude of EPC  $\lambda_{qv}$  of (b) type-I ort-MgB<sub>6</sub> and (f) type-I ort-CaB<sub>6</sub>. Phonon density of states (PhDOS) of (c) type-I ort-MgB<sub>6</sub> and (g) type-I ort-CaB<sub>6</sub>. Eliashberg spectral function  $\alpha^2 F(\omega)$  and cumulative frequency dependence of EPC  $\lambda(\omega)$  of (d) type-I ort-MgB<sub>6</sub> and (h) type-I ort-CaB<sub>6</sub>.

of type-I ort-TiB<sub>6</sub> and -YB<sub>6</sub>. However, for type-II ort-TiB<sub>6</sub> and type-III ort-YB<sub>6</sub>, the imaginary frequency disappears. A CDW phase transition exists for ort-TiB<sub>6</sub> and ort-YB<sub>6</sub>. For these two materials, the B<sub>z</sub> vibrations are mainly distributed in the frequency range below 600 cm<sup>-1</sup>, while the B<sub>xy</sub> vibration is distributed in the whole area of the BZ. For type-II ort-TiB<sub>6</sub>, there is a sharp phonon softening at the S point, caused by B<sub>z</sub> vibrations. The phonon modes (below 200 cm<sup>-1</sup>), dominated by B modes, contribute about 50% of the total EPC ( $\lambda = 0.92$ ). As shown in Fig. 7(c), the region with the largest EPC is around the S point. However, in the region around the  $\Gamma$  and X points, the EPC is very small. These results are consistent with the EPC  $\lambda_{qv}$  in Fig. 5(b). For type-III ort-YB<sub>6</sub>, there is a softened phonon mode at the Y point, mainly from the Ti<sub>xy</sub> vibrations, which exhibits strong EPC. About 80% of the total EPC ( $\lambda = 1.00$ ) arises from the phonon frequency range below 250 cm<sup>-1</sup>, which is mainly from the B<sub>z</sub> and Y<sub>xy</sub> vibrations. From the distribution map of EPC [see Fig. 7(d)], we find that the region with the largest EPC is around the

Y point, which is consistent with the EPC  $\lambda_{qv}$  in Fig. 5(f). The EPC values of 0.92 and 1.00 indicate that both type-II ort-TiB<sub>6</sub> and type-III ort-YB<sub>6</sub> belong to intermediate-coupling conventional superconductors. The calculated  $T_c$  are 16.9 and 17.4 K for type-II ort-TiB<sub>6</sub> and type-III ort-YB<sub>6</sub>, respectively.

Based on the elastic theory [76,77], for strict 2D materials, the out-of-plane acoustic (ZA) branch at the  $\Gamma$  point should be quadratic. We present in Fig. S11 [54] the enlarged figures of the ZA branches near the  $\Gamma$  point for hex-MgB<sub>6</sub>, hex-CaB<sub>6</sub>, hex-ScB<sub>6</sub>, and hex-TiB<sub>6</sub>. One can see that in the long-wavelength limit, the ZA branches for these monolayers are all quadratic, not linear dispersion. For example, for hex-CaB<sub>6</sub> [see Fig. S11(b) [54]], ZA is linear dispersion when  $\omega > 10$  cm<sup>-1</sup>. However, it becomes quadratic in the frequency range of  $\omega < 10$  cm<sup>-1</sup>. Actually, our studied MB<sub>6</sub> materials are composed of three atomic layers. The thickness effect (buckling) on the dispersion cannot be ignored. Thus, the ZA branch has some coupling with in-plane longitudinal and transversal acoustic (LA and TA) modes. When the in-plane

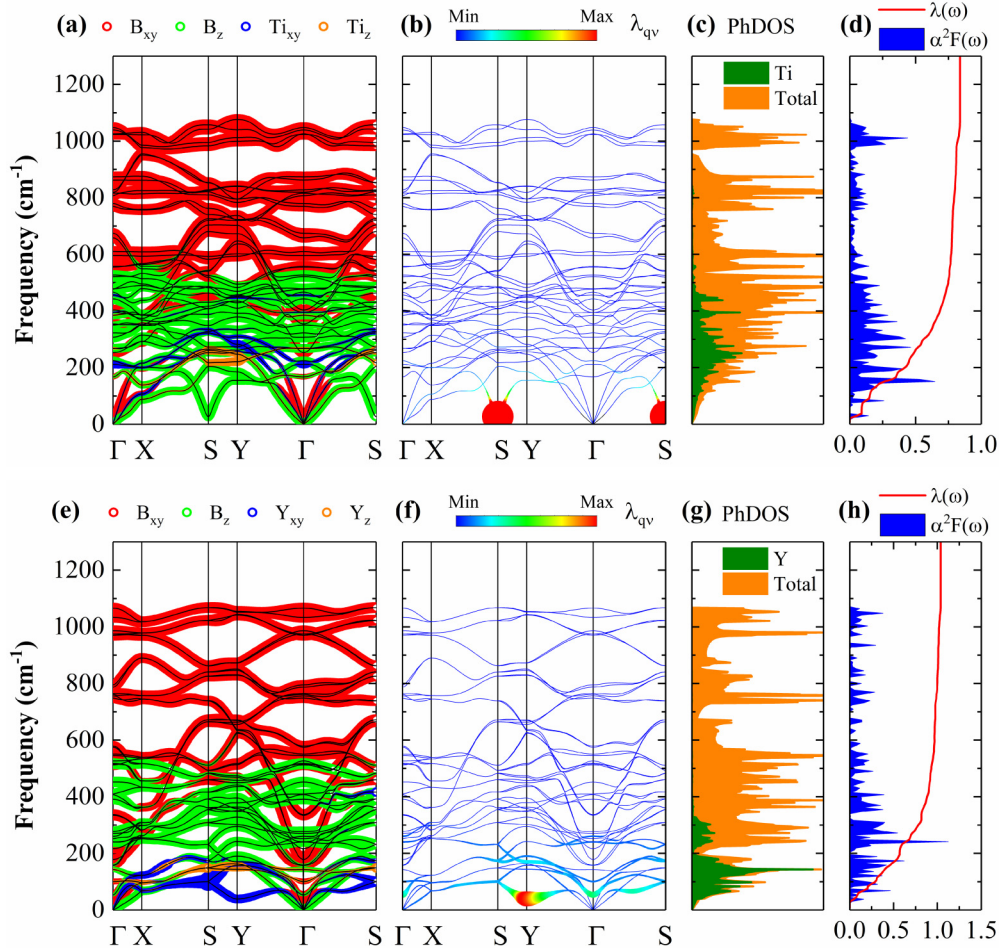


FIG. 5. Phonon dispersions weighted by the motion modes of B, M ( $M = \text{Ti}, \text{Y}$ ) atoms of (a) type-II ort-TiB<sub>6</sub> and (e) type-III ort-YB<sub>6</sub>. The red, green, blue, and orange hollow circles in (a) and (e) represent B horizontal, B vertical, M ( $M = \text{Ti}, \text{Y}$ ) horizontal, and M ( $M = \text{Ti}, \text{Y}$ ) vertical modes, respectively. Phonon dispersions weighted by the magnitude of EPC  $\lambda_{qv}$  of (b) type-II ort-TiB<sub>6</sub> and (f) type-III ort-YB<sub>6</sub>. Phonon density of states (PhDOS) of (c) type-II ort-TiB<sub>6</sub> and (g) type-III ort-YB<sub>6</sub>. Eliashberg spectral function  $\alpha^2F(\omega)$  and cumulative frequency dependence of EPC  $\lambda(\omega)$  of (d) type-II ort-TiB<sub>6</sub> and (h) type-III ort-YB<sub>6</sub>.

size is comparable to the thickness of 2D material, the corresponding system appears bulklike and the corresponding ZA dispersion is expected to be nearly linear due to this coupling [78]. However, the thickness effect would fade away at long enough wavelength. Thus, in the long-wavelength limit, the ZA branch has quadratic rather than linear dispersion for these hex- $MB_6$  ( $M = \text{Mg}, \text{Ca}, \text{Sc}, \text{Ti}$ ).

For these hex- $MB_6$  ( $M = \text{Mg}, \text{Ca}, \text{Sc}, \text{Ti}$ ), the B<sub>z</sub> vibrations are mainly distributed in the frequency range of 0–500 cm<sup>-1</sup>, while the B<sub>xy</sub> vibrations are distributed in whole area of the BZ. For hex-MgB<sub>6</sub>, the Mg vibrations are mainly distributed in the frequency range of 200–400 cm<sup>-1</sup>. About 75% of the total EPC ( $\lambda = 0.46$ ) arises from the phonon frequency range of  $\sim 180$ –400 cm<sup>-1</sup>, which is mainly from the B<sub>z</sub> vibrations. As shown in Fig. 7(e), the region with the largest EPC is around the  $M$  point, and there is also strong EPC in the region around the  $K$  point. However, in the region around the  $\Gamma$  point, the EPC is very small. These results are consistent with the EPC  $\lambda_{qv}$  in Fig. 6(b). For hex-CaB<sub>6</sub>, the Ca vibrations are mainly distributed in the low frequency below 220 cm<sup>-1</sup>. There are two softened acoustic branches with the phonon frequency below 150 cm<sup>-1</sup>, which are mainly from the Ca<sub>xy</sub> vibrations.

Here, the softened phonon modes result in a strong EPC, which account for 39% the total EPC ( $\lambda = 0.87$ ). The phonon modes in the frequency range of 200–500 cm<sup>-1</sup>, mainly associated with the B<sub>z</sub> vibrations, contribute 46% to the total EPC ( $\lambda = 0.87$ ). As shown in Fig. 7(f), the region with the largest EPC is along the  $\Gamma$ - $K$  line, and there is strong EPC in the whole BZ, which is consistent with the EPC  $\lambda_{qv}$  in Fig. 6(f). For hex-ScB<sub>6</sub>, the Sc vibrations are mainly distributed in the frequency range of 150–300 cm<sup>-1</sup>. There are two softened acoustic branches; one is softening along the  $M$ - $K$  line, the other around the  $K$  point. About 67% of the total EPC ( $\lambda = 0.60$ ) arises from these two softened phonon modes, which are mainly from the B<sub>z</sub> vibrations. From the distribution map of EPC [see Fig. 7(g)], we find that the region with the largest EPC is along the  $M$ - $K$  line and there is also strong EPC around the  $K$  point, which is consistent with the EPC  $\lambda_{qv}$  in Fig. 6(j). For hex-TiB<sub>6</sub>, the Ti vibrations are mainly distributed in the frequency range of 100–300 cm<sup>-1</sup>. The softened phonon modes (100–300 cm<sup>-1</sup>), mainly associated with the B<sub>xy</sub> and B<sub>z</sub> vibrations, contribute about 68% of the total EPC ( $\lambda = 0.40$ ). The EPC is mainly in the region around the  $K$  point, which can be verified by the distribution map of

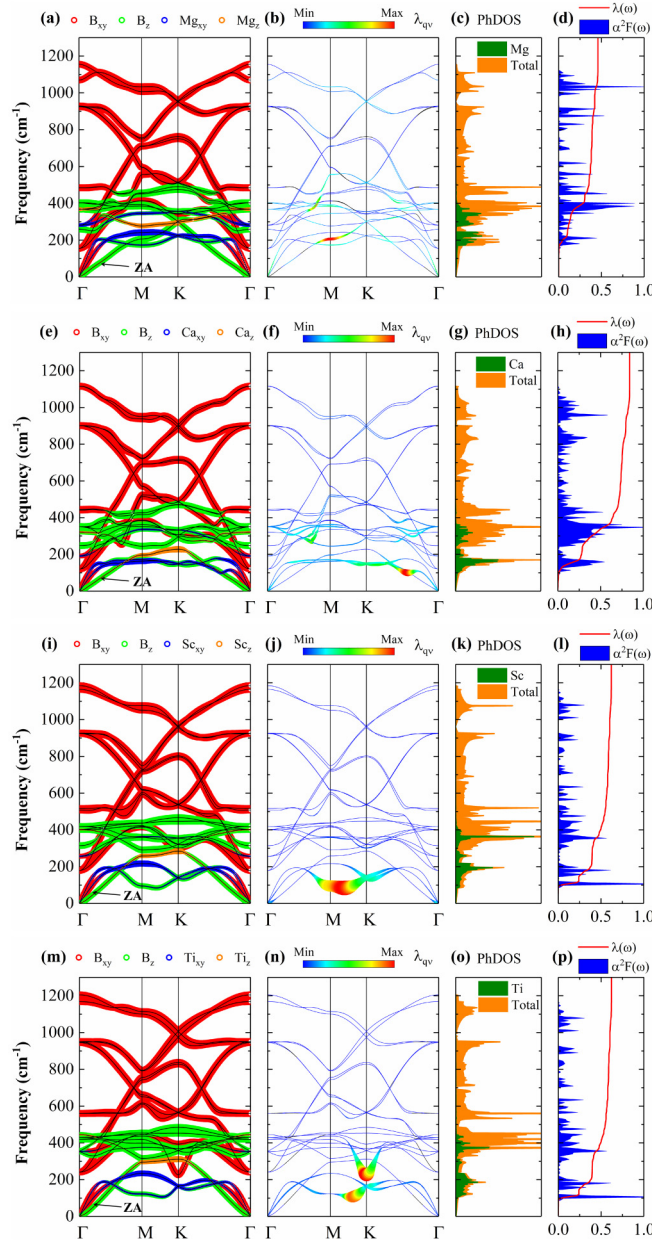


FIG. 6. Phonon dispersions weighted by the motion modes of B, M ( $M = \text{Mg, Ca, Sc, Ti}$ ) atoms of (a) hex-MgB<sub>6</sub>, (e) hex-CaB<sub>6</sub>, (i) hex-ScB<sub>6</sub>, and (m) hex-TiB<sub>6</sub>. The red, green, blue, and orange hollow circles represent B horizontal, B vertical,  $M$  ( $M = \text{Mg, Ca, Sc, Ti}$ ) horizontal, and  $M$  ( $M = \text{Mg, Ca, Sc, Ti}$ ) vertical modes, respectively. Phonon dispersions weighted by the magnitude of EPC  $\lambda_{qv}$  of (b) hex-MgB<sub>6</sub>, (f) hex-CaB<sub>6</sub>, (j) hex-ScB<sub>6</sub>, and (n) hex-TiB<sub>6</sub>. Phonon density of states (PhDOS) of (c) hex-MgB<sub>6</sub>, (g) hex-CaB<sub>6</sub>, (k) hex-ScB<sub>6</sub>, and (o) hex-TiB<sub>6</sub>. Eliashberg spectral function  $\alpha^2F(\omega)$  and cumulative frequency dependence of EPC  $\lambda(\omega)$  of (d) hex-MgB<sub>6</sub>, (h) hex-CaB<sub>6</sub>, (l) hex-ScB<sub>6</sub>, and (p) hex-TiB<sub>6</sub>.

EPC shown in Fig. 7(h). The EPC values of 0.46, 0.87, 0.60, and 0.40 indicate that the hex-MgB<sub>6</sub>, hex-ScB<sub>6</sub>, and hex-TiB<sub>6</sub> belong to weak-coupling conventional superconductors and the hex-CaB<sub>6</sub> belongs to intermediate-coupling conventional superconductors. Then, the calculated  $T_c$  are 4.7, 22.6, 6.7,

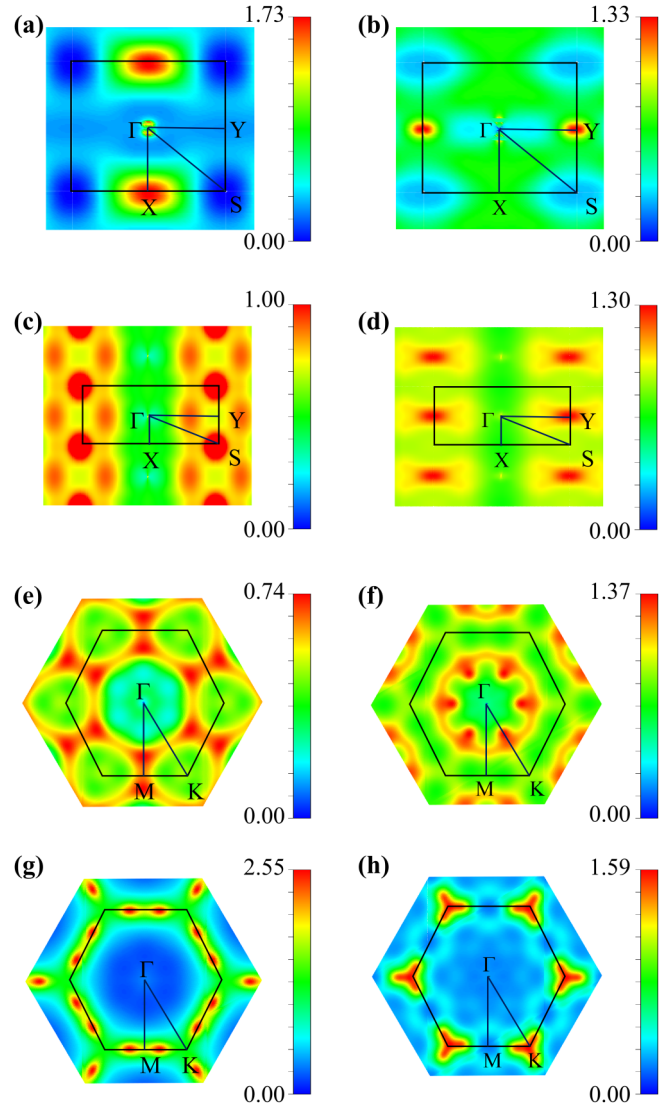


FIG. 7. The integrated EPC distributions in the BZs for (a) type-I ort-MgB<sub>6</sub>, (b) type-I ort-CaB<sub>6</sub>, (c) type-II ort-TiB<sub>6</sub>, (d) type-III ort-YB<sub>6</sub>, (e) hex-MgB<sub>6</sub>, (f) hex-CaB<sub>6</sub>, (g) hex-ScB<sub>6</sub>, and (h) hex-TiB<sub>6</sub>.

and 1.4 K for hex-MgB<sub>6</sub>, hex-CaB<sub>6</sub>, hex-ScB<sub>6</sub>, and hex-TiB<sub>6</sub>, respectively.

## E. Discussion

We find that for our studied MB<sub>6</sub> monolayers, the softened phonon modes always result in strong EPC, which is similar to the borophenes [79], 2D  $\beta_0$ -PC [31], 2D Mo<sub>2</sub>B<sub>2</sub> [33], and 2D W<sub>2</sub>B<sub>2</sub> [34]. We present in Fig. S12 [54] the phonon linewidth distributions in the BZs for these MB<sub>6</sub> monolayers. According to Eq. (1), the EPC  $\lambda_{qv}$  is proportional to phonon linewidth  $\gamma_{qv}$  and inversely proportional to the square of phonon frequency  $\omega_{qv}$ . Therefore, large phonon linewidth and low phonon frequency will lead to strong EPC. As shown in Fig. S12 [54], the phonon modes at the high-frequency region tend to have very large phonon linewidth, but the corresponding EPC is very small owing to the large frequency. In the low-frequency region, the phonon width is more distributed on the softened acoustic branches whose phonon frequency

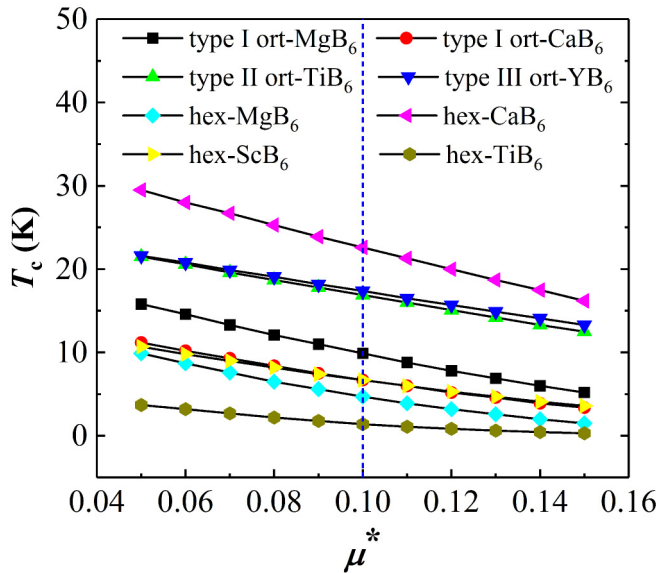


FIG. 8. Evaluated  $T_c$  of our studied  $MB_6$  monolayers as a function of Coulomb pseudopotential  $\mu^*$ . Vertical line marks the value  $\mu^* = 0.10$  used in this work.

is very small. Thus, the softened acoustic branches always result in very strong EPC  $\lambda_{qv}$ . Then, according to Eqs. (3) and (4), we can deduce that the softened phonon mode has a great contribution to the EPC constant  $\lambda$ . However, we cannot ignore the limitations of the perturbative method used in this work, which adopts the harmonic approximation. The

softened phonon modes in these  $MB_6$  monolayers may be caused by the absence of dealing with anharmonic effects. For some materials, such as Palladium-Hydride compounds [80], the phonon spectra are renormalized by anharmonicity far beyond the perturbative regime. Besides, the EPC constant  $\lambda$  and  $T_c$  can also be overestimated due to ignoring anharmonicity effects. While the method used in this work enables us to identify interesting candidates for superconductivity, more sophisticated techniques such as stochastic self-consistent harmonic approximation (SSCHA) [80] or SuperConducting DFT (SCDFT) [81,82] might be necessary to describe superconductivity more accurately. In particular, anharmonicity might be necessary to treat the softened phonon modes. We will discuss these in the future work.

As we know,  $\mu^*$  is an empirical parameter which has a close relationship with  $T_c$ . In order to know clearly the influence of  $\mu^*$  on  $T_c$ , we investigate the  $T_c$  of these  $MB_6$  monolayers as a function of  $\mu^*$ . The value of  $\mu^*$  are considered in the range of 0.05–0.15. As shown in Fig. 8, for all the  $MB_6$  materials, the  $T_c$  decreases monotonically with the increasing of  $\mu^*$ . For hex-CaB<sub>6</sub>, the  $T_c$  is largest (29.5 K) when  $\mu^*$  is 0.05. As  $\mu^*$  increases from 0.05 to 0.15,  $T_c$  decreases from 29.5 to 15.1 K.

In Table III, we list the superconducting parameters of  $\mu^*$ ,  $N(E_F)$ ,  $\omega_{ln}$ , EPC constant  $\lambda$ , and  $T_c$  for our calculated eight 2D  $MB_6$  and other intrinsic borophenes [24,26] and 2D metal borides superconductors [32–35,45]. Among the 2D  $MB_6$  we studied, hex-CaB<sub>6</sub> has the largest  $N(E_F)$  in the hexagonal  $MB_6$  while type-II ort-TiB<sub>6</sub> and type-III ort-YB<sub>6</sub> have the largest  $N(E_F)$  in the orthogonal  $MB_6$ . These three

TABLE III. Superconducting parameters of  $\mu^*$ ,  $N(E_F)$  (states/spin/Ry/unit cell),  $\omega_{ln}$  (K), EPC constant  $\lambda$ , and  $T_c$  (K) for our calculated 2D  $MB_6$  and other intrinsic borophenes and 2D metal borides superconductors. The theoretical and experimental data of bulk  $Pm\text{-}3m\text{-}YB_6$  are also presented.

Materials	$\mu^*$	$N(E_F)$	$\omega_{ln}$	$\lambda$	$T_c$	Refs.
Type-I ort-MgB <sub>6</sub>	0.1	8.9	447.2	0.59	9.9	this work
Type-I ort-CaB <sub>6</sub>	0.1	9.7	347.4	0.57	6.7	this work
hex-MgB <sub>6</sub>	0.1	7.9	559.6	0.46	4.7	this work
hex-CaB <sub>6</sub>	0.1	11.7	413.8	0.87	22.6	this work
hex-ScB <sub>6</sub>	0.1	8.9	297.8	0.60	6.7	this work
hex-TiB <sub>6</sub>	0.1	8.6	324.6	0.40	1.4	this work
Type-II ort-TiB <sub>6</sub>	0.1	27.6	276.8	0.92	16.9	this work
Type-III ort-YB <sub>6</sub>	0.1	28.3	250.2	1.00	17.4	this work
$B_\Delta/B_\square/B_\diamond$	0.1			1.1/0.8/0.6	21/16/12	[24]
$\beta_{12}$	0.1			0.69	14	[26]
ort-MgB <sub>6</sub>	0.1		554.2	0.49	6.0	[32]
ort-AlB <sub>6</sub>	0.05	6.41	345.2	0.36	4.7	[35]
ort-GaB <sub>6</sub>	0.1	6.40	490.3	0.39	1.67	[45]
hex-GaB <sub>6</sub>	0.1	7.79	436.1	0.68	14.02	[45]
ort-InB <sub>6</sub>	0.1	8.69	471.2	0.55	7.77	[45]
hex-InB <sub>6</sub>	0.1	9.43	154.1	0.67	4.83	[45]
tetr-Mo <sub>2</sub> B <sub>2</sub>	0.1	16.02	344.84	0.49	3.9	[33]
tri-Mo <sub>2</sub> B <sub>2</sub>	0.1	16.81	295.0	0.3	0.2	[33]
tetr-W <sub>2</sub> B <sub>2</sub>	0.1	12.46	232.4	0.69	7.8	[34]
hex-W <sub>2</sub> B <sub>2</sub>	0.1	13.60	232.2	0.43	1.5	[34]
<i>Pm</i> -3 <i>m</i> -YB <sub>6</sub>	0.1	1.36	72.31	0.87	7.47	[84]
<sup>a</sup> <i>Pm</i> -3 <i>m</i> -YB <sub>6</sub>					7.2	[44]

<sup>a</sup>These are experimental data.

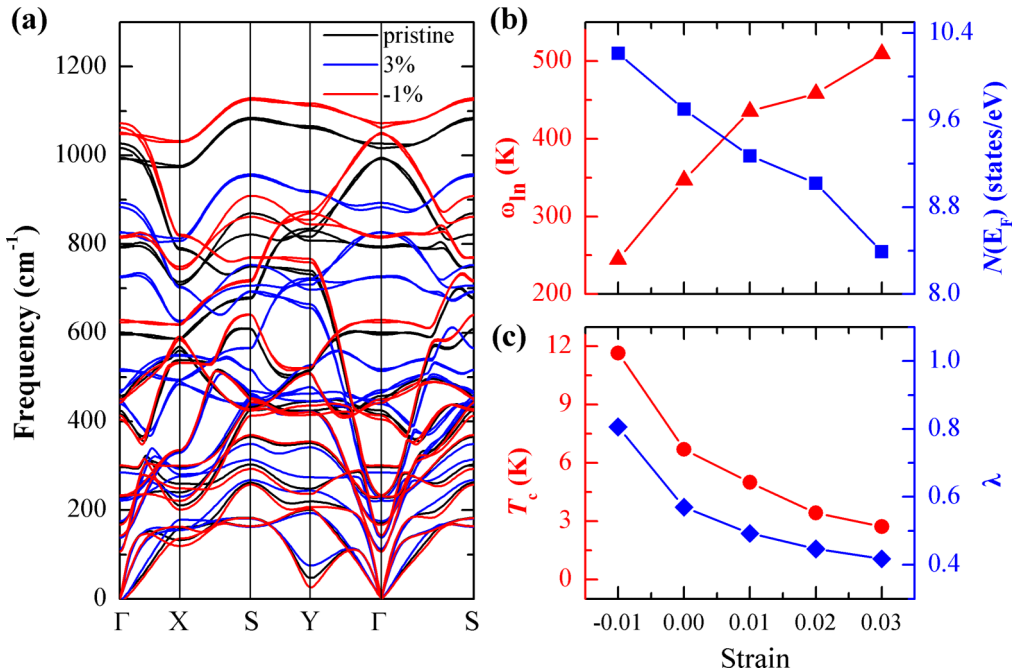


FIG. 9. (a) Phonon dispersions, (b) logarithmically averaged phonon frequency  $\omega_{\ln}$  (red) and  $N(E_F)$  (blue), (c)  $T_c$  (red) and EPC constant  $\lambda$  (blue) under different strains for type-I ort-CaB<sub>6</sub>.

materials possess the largest values of  $T_c$ . This indicates that the density of states at the Fermi level has a positive effect on superconductivity. The EPC constant  $\lambda$  is in the range of 0.40–1.00 and the  $T_c$  is in the range of 1.4–22.6 K. While the hex-TiB<sub>6</sub> has the smallest  $T_c$  (1.4 K) with the smallest EPC constant ( $\lambda = 0.40$ ), the hex-CaB<sub>6</sub> possesses the largest  $T_c$  of 22.6 K with a larger EPC constant ( $\lambda = 0.87$ ). Besides, hex-MgB<sub>6</sub>, which has the second smallest EPC constant ( $\lambda = 0.46$ ), also has a small  $T_c$  (4.7 K). Type-II ort-TiB<sub>6</sub> and type-III ort-YB<sub>6</sub>, which possess the largest EPC constant ( $\lambda = 0.92$  and 1.00, respectively), hold large  $T_c$  (16.9 and 17.4 K, respectively). Type-I ort-MgB<sub>6</sub> and -CaB<sub>6</sub> have almost the same value of EPC constant ( $\lambda = 0.59$  and 0.57, respectively). However, the  $T_c$  of the ort-MgB<sub>6</sub> (9.9 K) is larger than that of the ort-CaB<sub>6</sub> (7.1 K), which is mainly due to the larger  $\omega_{\ln}$  for ort-MgB<sub>6</sub>. The same phenomenon also occurs on hex-MgB<sub>6</sub> and hex-CaB<sub>6</sub>. We find that the above laws are consistent with the well-known empirical principles of conventional superconductivity named the Matthias rules [83]. Some conclusions are summarized as follows: (1) EPC constant  $\lambda$  plays an important role in the superconductivity. Large values of  $\lambda$  often leads to large  $T_c$ . (2) Materials with softened acoustic branches in the phonon spectrum are more likely to have superconductivity. (3) The electronic density of states at the Fermi level  $N(E_F)$  and the logarithmic average frequency  $\omega_{\ln}$  have positive effect on superconductivity. To have a more comprehensive view of our predicted 2D MB<sub>6</sub>, we compare their EPC constants  $\lambda$  and  $T_c$  with the reported borophenes [24,26] and 2D metal borides [32–35,45]. Among all the materials listed in Table III, our studied hex-CaB<sub>6</sub> possesses the largest  $T_c$  (22.6 K). In addition to hex-CaB<sub>6</sub>, our obtained type-II ort-TiB<sub>6</sub> and type-III ort-YB<sub>6</sub> also have large  $T_c$  of 16.9 and 17.4 K, respectively, which is larger than that of B<sub>6</sub> [24],  $\beta_{12}$  [26], ort-AlB<sub>6</sub> [35], ort-/hex-GaB<sub>6</sub> [45],

ort-/hex-InB<sub>6</sub> [45], Mo<sub>2</sub>B<sub>2</sub> [33], and W<sub>2</sub>B<sub>2</sub> [34], while smaller than that of B<sub>6</sub> [24]. The  $T_c$  of our studied materials, except for hex-MgB<sub>6</sub> and hex-TiB<sub>6</sub>, is greater than that of ort-AlB<sub>6</sub> [35]. Compared with bulk YB<sub>6</sub> [44,84], type-III ort-YB<sub>6</sub> has larger  $N(E_F)$  and EPC constant, which leads to a larger  $T_c$ . The different arrangement of atoms in the crystal cell results in the difference of superconductivity between 2D and bulk YB<sub>6</sub>.

## F. Strain engineering

When these 2D MB<sub>6</sub> are grown on substrates, strains will be introduced, therefore, the superconducting properties should be affected. Therefore, we apply strain by changing the lattice parameters to investigate the effect of strains on the EPC and superconducting properties of these 2D materials. Here, we choose type-I ort-CaB<sub>6</sub> and the hex-CaB<sub>6</sub> as the representatives to study. First, we discuss the dynamical stability of type-I ort-CaB<sub>6</sub> and hex-CaB<sub>6</sub> under different strains. The equibiaxial tensile and compressive strains have been applied on these two configurations. The positive value of  $\varepsilon$  represents tensile strain while the negative value represents compressive strain. For type-I ort-CaB<sub>6</sub>, we find that it is only dynamically stable under the strain region of  $-1\% \leq \varepsilon \leq 3\%$ , indicating that it can withstand up to 1% compressive strain and 3% tensile strain. The phonon dispersions under  $\varepsilon = -1\%$ , 0, and 3% are displayed in Fig. 9(a). We find that the compression strain makes the phonon frequency at low frequency ( $<500\text{ cm}^{-1}$ ) lower down, but those at high frequency ( $>500\text{ cm}^{-1}$ ) higher up. When tensile strain is applied, the trends of the phonon frequency change are opposite. As shown in Figs. 9(b) and 9(c), when the strain  $\varepsilon$  increases from  $-1\%$  to  $3\%$ , the logarithmically averaged phonon frequency  $\omega_{\ln}$  increases linearly, whereas the  $N(E_F)$ , the EPC constant  $\lambda$ , and

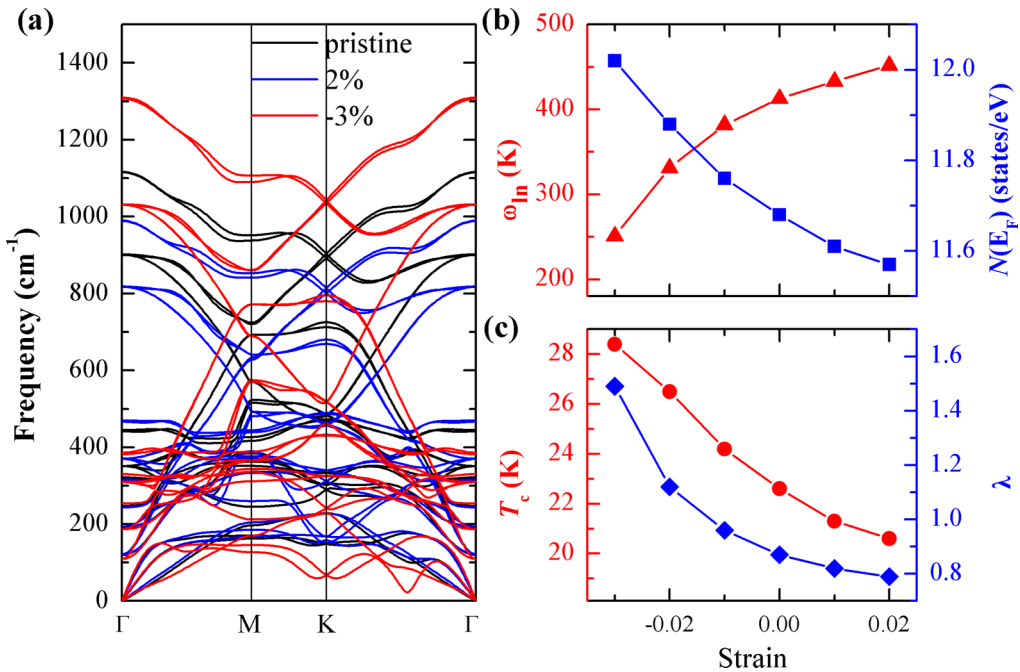


FIG. 10. (a) Phonon dispersions, (b) logarithmically averaged phonon frequency  $\omega_{\ln}$  (red) and  $N(E_F)$  (blue), (c)  $T_c$  (red) and EPC constant  $\lambda$  (blue) under different strains for hex-CaB<sub>6</sub>.

the  $T_c$  decreases linearly. Under compressive strain of  $-1\%$ , the largest  $T_c$  of about 12 K is obtained.

For hex-CaB<sub>6</sub>, it is only dynamically stable under the strain region of  $-3\% \leq \varepsilon \leq 2\%$ , indicating that it can bear more compression strain than type-I ort-CaB<sub>6</sub>. The phonon dispersions under  $\varepsilon = -3\%$ , 0, and 2% are displayed in Fig. 10(a). Like type-I ort-CaB<sub>6</sub>, the compression strain makes the phonon frequency at low frequency ( $<500 \text{ cm}^{-1}$ ) lower down, but those at high frequency ( $>500 \text{ cm}^{-1}$ ) higher up. As shown in Figs. 10(b) and 10(c), when the strain  $\varepsilon$  increases from  $-3\%$  to 2%, the logarithmically averaged phonon frequency  $\omega_{\ln}$  increases linearly, whereas the  $N(E_F)$ , the EPC constant  $\lambda$ , and the  $T_c$  are almost linearly reduced. Under the maximum compressive strain of  $\varepsilon = -3\%$ , the  $T_c$  can be modulated up to about 28.4 K. Therefore, the compressive strain can strengthen the EPC and increase the  $T_c$  of both type-I ort-CaB<sub>6</sub> and hex-CaB<sub>6</sub>.

#### IV. CONCLUSION

In our present work, by combining the crystal structure search as well as systematic first-principles calculations, we predict a series of 2D metal borides, including orthorhombic  $MB_6$  ( $M = Mg, Ca, Ti, Y$ ) and hexagonal  $MB_6$  ( $M = Mg, Ca, Sc, Ti$ ), and investigate their geometrical structures, bonding properties, electronic structures, mechanical properties, phonon dispersions, dynamic stability, CDW phase transition, EPC, superconducting properties and so on. These ort- $MB_6$  and hex- $MB_6$  structures belong to the orthogonal  $Pnmm$  and the hexagonal  $P6/mmm$  space group, respectively, which consist of one layer of metal atoms and two layers of B atoms. Some of these materials contain covalent and ionic bonds, while others also have metal bonds in addition to the above two bonds. Our AIMD simulations show that these 2D  $MB_6$

well maintain their original configurations up to about 1000 or 700 K (only for hex-MgB<sub>6</sub>), indicating the excellent thermodynamic stability of these  $MB_6$  monolayers. No imaginary modes in the entire BZ proves that they are dynamically stable. Our calculated elastic constants clearly illustrate that these  $MB_6$  monolayers are all mechanically stable. The strong B-B bonding enable large values of  $C_{11}$ . Thus, once our predicted 2D  $MB_6$  being synthesized in experiments, good stability is expected.

Interestingly, there is CDW phase transition for ort-TiB<sub>6</sub> from type-I to type-II  $2 \times 1$  supercell structure and for ort-YB<sub>6</sub> from type-I to type-III  $2 \times 1$  supercell structure. Based upon the BCS theory, by analytically solving the McMillan-Allen-Dynes formula, we find that these eight 2D  $MB_6$  materials are all intrinsic phonon-mediated superconductors with the  $T_c$  in the range of 1.4 to 22.6 K. Among them, there are five weak-coupling conventional superconductors with small EPC constants  $\lambda$  (0.40–0.60), including type-I ort-MgB<sub>6</sub> and -CaB<sub>6</sub>, hex-MgB<sub>6</sub>, hex-ScB<sub>6</sub>, and hex-TiB<sub>6</sub>, while there are three intermediate-coupling conventional superconductors with large EPC constants  $\lambda$  (0.87–1.00), including hex-CaB<sub>6</sub>, type-II ort-TiB<sub>6</sub>, and type-III ort-YB<sub>6</sub>. The EPC is mainly governed by the B vibrations. The softened phonon modes play a critical role for the large EPC. We also study the effects of tensile/compressive strains on the superconducting properties of type-I ort-CaB<sub>6</sub> and hex-CaB<sub>6</sub>. Results show that compressive strains obviously enhance the EPC and increase the  $T_c$  for both type-I ort-CaB<sub>6</sub> and hex-CaB<sub>6</sub>, which is due to the lower acoustic-phonon branch being softened. A large  $T_c$  of 28.4 K for hex-CaB<sub>6</sub> is obtained.

Our findings in the present work enrich the database of 2D metal borides and may stimulate experimental synthesis of these materials and also 2D metal carbides and nitrides. The superconducting properties of these 2D  $MB_6$  supply

experiments another choice other than the 2D boron to realize superconducting monolayers in boron based 2D forms. After all, the thickness of these 2D  $MB_6$  is prior to borophene and their  $T_c$  are relatively high.

### ACKNOWLEDGMENTS

We acknowledge financial support from Guangdong Basic and Applied Basic Research Foundation under Grant No.

2019A1515110920 and the Ph.D. Start-up Fund of the Natural Science Foundation of Guangdong Province of China (Grant No. 2018A0303100013). B.-T.W. acknowledges financial support from the Natural Science Foundation of China (Grant No. 12074381) and the Program of State Key Laboratory of Quantum Optics and Quantum Optics Devices (Grant No. KF201904). The work was completed with the computational resources from the Supercomputer Centre of the China Spallation Neutron Source.

- [1] E. Dagotto, *Rev. Mod. Phys.* **66**, 763 (1994).
- [2] P. Dai, *Rev. Mod. Phys.* **87**, 855 (2015).
- [3] F. Giustino, *Rev. Mod. Phys.* **89**, 015003 (2017).
- [4] J. Nagamatsu, N. Nakagawa, T. Muranaka, Y. Zenitani, and J. Akimitsu, *Nature (London)* **410**, 63 (2001).
- [5] A. Y. Liu, I. I. Mazin, and J. Kortus, *Phys. Rev. Lett.* **87**, 087005 (2001).
- [6] A. Floris, G. Profeta, N. N. Lathiotakis, M. Lüders, M. A. L. Marques, C. Franchini, E. K. U. Gross, A. Continenza, and S. Massidda, *Phys. Rev. Lett.* **94**, 037004 (2005).
- [7] E. R. Margine and F. Giustino, *Phys. Rev. B* **87**, 024505 (2013).
- [8] A. Bhaumik, R. Sachan, and J. Narayan, *ACS Nano* **11**, 5351 (2017).
- [9] X. Liang, A. Bergara, L. Wang, B. Wen, Z. Zhao, X.-F. Zhou, J. He, G. Gao, and Y. Tian, *Phys. Rev. B* **99**, 100505(R) (2019).
- [10] Y. Li, J. Hao, H. Liu, Y. Li, and Y. Ma, *J. Chem. Phys.* **140**, 174712 (2014).
- [11] H. Liu, I. I. Naumov, R. Hoffmann, N. W. Ashcroft, and R. J. Hemley, *Proc. Natl. Acad. Sci. U.S.A.* **114**, 6990 (2017).
- [12] J. Bardeen, L. N. Cooper, and J. R. Schrieffer, *Phys. Rev.* **108**, 1175 (1957).
- [13] A. P. Drozdov, M. I. Eremets, I. A. Troyan, V. Ksenofontov, and S. I. Shylin, *Nature (London)* **525**, 73 (2015).
- [14] A. P. Drozdov, P. P. Kong, V. S. Minkov, S. P. Besedin, M. A. Kuzovnikov, S. Mozaffari, L. Balicas, F. F. Balakirev, D. E. Graf, V. B. Prakapenka, E. Greenberg, D. A. Knyazev, M. Tkacz, and M. I. Eremets, *Nature (London)* **569**, 528 (2019).
- [15] M. Somayazulu, M. Ahart, A. K. Mishra, Z. M. Geballe, M. Baldini, Y. Meng, V. V. Struzhkin, and R. J. Hemley, *Phys. Rev. Lett.* **122**, 027001 (2019).
- [16] T. Uchihashi, *Supercond. Sci. Technol.* **30**, 013002 (2016).
- [17] C. Brun, T. Cren, and D. Roditchev, *Supercond. Sci. Technol.* **30**, 013003 (2016).
- [18] C. Xu, L. Wang, Z. Liu, L. Chen, J. Guo, N. Kang, X.-L. Ma, H.-M. Cheng, and W. Ren, *Nat. Mater.* **14**, 1135 (2015).
- [19] B. M. Ludbrook, G. Levy, P. Nigge, M. Zonno, M. Schneider, D. J. Dvorak, C. N. Veenstra, S. Zhdanovich, D. Wong, P. Dosanjh, C. Straßer, A. Stöhr, S. Forti, C. R. Ast, U. Starke, and A. Damascelli, *Proc. Natl. Acad. Sci. U.S.A.* **112**, 11795 (2015).
- [20] X. Xi, Z. Wang, W. Zhao, J.-H. Park, K. T. Law, H. Berger, L. Forró, J. Shan, and K. F. Mak, *Nat. Phys.* **12**, 139 (2016).
- [21] L. Zhu, Q.-Y. Li, Y.-Y. Lv, S. Li, X.-Y. Zhu, Z.-Y. Jia, Y. B. Chen, J. Wen, and S.-C. Li, *Nano Lett.* **18**, 6585 (2018).
- [22] M. Liao, Y. Zang, Z. Guan, H. Li, Y. Gong, K. Zhu, X.-P. Hu, D. Zhang, Y. Xu, Y.-Y. Wang, K. He, X.-C. Ma, S.-C. Zhang, and Q.-K. Xue, *Nat. Phys.* **14**, 344 (2018).
- [23] Y. Cao, V. Fatemi, S. Fang, K. Watanabe, T. Taniguchi, E. Kaxiras, and P. Jarillo-Herrero, *Nature (London)* **556**, 43 (2018).
- [24] E. S. Penev, A. Kutana, and B. I. Yakobson, *Nano Lett.* **16**, 2522 (2016).
- [25] M. Gao, Q.-Z. Li, X.-W. Yan, and J. Wang, *Phys. Rev. B* **95**, 024505 (2017).
- [26] C. Cheng, J.-T. Sun, H. Liu, H.-X. Fu, J. Zhang, X.-R. Chen, and S. Meng, *2D Mater.* **4**, 025032 (2017).
- [27] M. Gao, X.-W. Yan, J. Wang, Z.-Y. Lu, and T. Xiang, *Phys. Rev. B* **100**, 024503 (2019).
- [28] H.-Y. Lu, Y. Yang, L. Hao, W.-S. Wang, L. Geng, M. Zheng, Y. Li, N. Jiao, P. Zhang, and C. S. Ting, *Phys. Rev. B* **101**, 214514 (2020).
- [29] E. R. Margine and F. Giustino, *Phys. Rev. B* **90**, 014518 (2014).
- [30] C. Si, Z. Liu, W. Duan, and F. Liu, *Phys. Rev. Lett.* **111**, 196802 (2013).
- [31] B.-T. Wang, P.-F. Liu, T. Bo, W. Yin, O. Eriksson, J. Zhao, and F. Wang, *Phys. Chem. Chem. Phys.* **20**, 12362 (2018).
- [32] J.-H. Liao, Y.-C. Zhao, Y.-J. Zhao, H. Xu, and X.-B. Yang, *Phys. Chem. Chem. Phys.* **19**, 29237 (2017).
- [33] L. Yan, T. Bo, P.-F. Liu, B.-T. Wang, Y.-G. Xiao, and M.-H. Tang, *J. Mater. Chem. C* **7**, 2589 (2019).
- [34] L. Yan, T. Bo, W. Zhang, P.-F. Liu, Z. Lu, Y.-G. Xiao, M.-H. Tang, and B.-T. Wang, *Phys. Chem. Chem. Phys.* **21**, 15327 (2019).
- [35] B. Song, Y. Zhou, H.-M. Yang, J.-H. Liao, L.-M. Yang, X.-B. Yang, and E. Ganz, *J. Am. Chem. Soc.* **141**, 3630 (2019).
- [36] B.-T. Wang, P.-F. Liu, J.-J. Zheng, W. Yin, and F. Wang, *Phys. Rev. B* **98**, 014514 (2018).
- [37] F. Weber, S. Rosenkranz, J.-P. Castellan, R. Osborn, R. Hott, R. Heid, K.-P. Bohnen, T. Egami, A. H. Said, and D. Reznik, *Phys. Rev. Lett.* **107**, 107403 (2011).
- [38] J. Bekaert, M. Petrov, A. Aperis, P. M. Oppeneer, and M. V. Milošević, *Phys. Rev. Lett.* **123**, 077001 (2019).
- [39] J.-J. Zhang, B. Gao, and S. Dong, *Phys. Rev. B* **93**, 155430 (2016).
- [40] J.-J. Zhang, Y. Zhang, and S. Dong, *Phys. Rev. Materials* **2**, 126004 (2018).
- [41] C. Cheng, J.-T. Sun, M. Liu, X.-R. Chen, and S. Meng, *Phys. Rev. Materials* **1**, 074804 (2017).
- [42] J.-J. Zhang and S. Dong, *J. Chem. Phys.* **146**, 034705 (2017).
- [43] L. Zhang, Y. Wang, J. Lv, and Y. Ma, *Nat. Rev. Mater.* **2**, 17005 (2017).
- [44] R. Lortz, Y. Wang, U. Tutsch, S. Abe, C. Meingast, P. Popovich, W. Knafo, N. Shitsevalova, Y. B. Paderno, and A. Junod, *Phys. Rev. B* **73**, 024512 (2006).

- [45] L. Yan, T. Bo, P.-F. Liu, L. Zhou, J. Zhang, M.-H. Tang, Y.-G. Xiao, and B.-T. Wang, *J. Mater. Chem. C* **8**, 1704 (2020).
- [46] Y. Wang, J. Lv, L. Zhu, and Y. Ma, *Phys. Rev. B* **82**, 094116 (2010).
- [47] Y. Wang, J. Lv, L. Zhu, and Y. Ma, *Comput. Phys. Commun.* **183**, 2063 (2012).
- [48] Y. Wang, M. Miao, J. Lv, L. Zhu, K. Yin, H. Liu, and Y. Ma, *J. Chem. Phys.* **137**, 224108 (2012).
- [49] G. Kresse and J. Furthmüller, *Phys. Rev. B* **54**, 11169 (1996).
- [50] J. P. Perdew, K. Burke, and M. Ernzerhof, *Phys. Rev. Lett.* **77**, 3865 (1996).
- [51] P. E. Blöchl, *Phys. Rev. B* **50**, 17953 (1994).
- [52] M. Fuchs and M. Scheffler, *Comput. Phys. Commun.* **119**, 67 (1999).
- [53] P. Giannozzi, S. Baroni, N. Bonini, M. Calandra, R. Car, C. Cavazzoni, D. Ceresoli, G. L Chiarotti, M. Cococcioni, I. Dabo, A. D. Corso, S. Gironcoli, S. Fabris, G. Fratesi, R. Gebauer, U. Gerstmann, C. Gougaussis, A. Kokalj, M. Lazzeri, L. Martin-Samos *et al.*, *J. Phys.: Condens. Matter* **21**, 395502 (2009).
- [54] See Supplemental Material at <http://link.aps.org/supplemental/10.1103/PhysRevMaterials.4.114802> for (I) convergence test of the  $q$ -point meshes, (II) the description of  $\mu^*$ , (III) the dynamically unstable 2D  $MB_6$ , (IV) electron localization function (ELF) of the  $MB_6$  monolayers, (V) snapshots and variation of the free energy for the 2D  $MB_6$  in the AIMD simulations from 300 to 1000 K, (VI) the enlarged figures of ZA branches near the  $\Gamma$  point for hex-MgB<sub>6</sub>, hex-CaB<sub>6</sub>, hex-ScB<sub>6</sub>, and hex-TiB<sub>6</sub>, (VII) phonon linewidth for the  $MB_6$  monolayers, (VIII) results of hex-CaB<sub>6</sub> with and without the flag `assume_isolated = "2D"`, and (IX) the structural information of  $MB_6$  and the details of the calculations and the results.
- [55] S. Baroni, S. de Gironcoli, A. Dal Corso, and P. Giannozzi, *Rev. Mod. Phys.* **73**, 515 (2001).
- [56] W. L. McMillan, *Phys. Rev.* **167**, 331 (1968).
- [57] P. B. Allen, *Phys. Rev. B* **6**, 2577 (1972).
- [58] P. B. Allen and R. C. Dynes, *Phys. Rev. B* **12**, 905 (1975).
- [59] C. F. Richardson and N. W. Ashcroft, *Phys. Rev. Lett.* **78**, 118 (1997).
- [60] Y. Zhao, S. Zeng, and J. Ni, *Appl. Phys. Lett.* **108**, 242601 (2016).
- [61] R. C. Xiao, D. F. Shao, W. J. Lu, H. Y. Lv, J. Y. Li, and Y. P. Sun, *Appl. Phys. Lett.* **109**, 122604 (2016).
- [62] Y. Sun, J. Lv, Y. Xie, H. Liu, and Y. Ma, *Phys. Rev. Lett.* **123**, 097001 (2019).
- [63] X. Wu, J. Dai, Y. Zhao, Z. Zhuo, J. Yang, and X. C. Zeng, *ACS Nano* **6**, 7443 (2012).
- [64] S.-Y. Xie, X.-B. Li, W. Q. Tian, N.-K. Chen, Y. Wang, S. Zhang, and H.-B. Sun, *Phys. Chem. Chem. Phys.* **17**, 1093 (2015).
- [65] A. Savin, R. Nesper, S. Wengert, and T. F. Fässler, *Angew. Chem. Int. Edit.* **36**, 1808 (1997).
- [66] W. Tang, E. Sanville, and G. Henkelman, *J. Phys.: Condens. Matter* **21**, 084204 (2009).
- [67] L. M. Yang, V. Bačić, I. A. Popov, A. I. Boldyrev, T. Heine, T. Frauenheim, and E. Ganz, *J. Am. Chem. Soc.* **137**, 2757 (2015).
- [68] B. Feng, B. Fu, S. Kasamatsu, S. Ito, P. Cheng, C.-C. Liu, Y. Feng, S. Wu, S. K. Mahatha, P. Sheverdyeva, P. Moras, M. Arita, O. Sugino, T.-C. Chiang, K. Shimada, K. Miyamoto, T. Okuda, K. Wu, L. Chen, Y. Yao, and I. Matsuda, *Nat. Commun.* **8**, 1007 (2017).
- [69] L.-M. Yang, I. A. Popov, T. Frauenheim, A. I. Boldyrev, T. Heine, V. Bačić, and E. Ganz, *Phys. Chem. Chem. Phys.* **17**, 26043 (2015).
- [70] L.-M. Yang, I. A. Popov, A. I. Boldyrev, T. Heine, T. Frauenheim, and E. Ganz, *Phys. Chem. Chem. Phys.* **17**, 17545 (2015).
- [71] F. Mouhat and F.-X. Coudert, *Phys. Rev. B* **90**, 224104 (2014).
- [72] S. Zhang, J. Zhou, Q. Wang, X. Chen, Y. Kawazoe, and P. Jena, *Proc. Natl. Acad. Sci. U.S.A.* **112**, 2372 (2015).
- [73] C. Lee, X. Wei, J. W. Kysar, and J. Hone, *Science* **321**, 385 (2008).
- [74] R. C. Andrew, R. E. Mapasha, A. M. Ukpong, and N. Chetty, *Phys. Rev. B* **85**, 125428 (2012).
- [75] W. Jiang, M. Kang, H. Huang, H. Xu, T. Low, and F. Liu, *Phys. Rev. B* **99**, 125131 (2019).
- [76] G. N. Virgin, *Vibration of Axially-Loaded Structures* (Cambridge University Press, Cambridge, UK, 2007).
- [77] J. Carrete, W. Li, L. Lindsay, D. A. Broido, L. J. Gallego, and N. Mingo, *Mater. Res. Lett.* **4**, 204 (2016).
- [78] Y. D. Kuang, L. Lindsay, S. Q. Shi, and G. P. Zheng, *Nanoscale* **8**, 3760 (2016).
- [79] Y. Zhao, S. Zeng, C. Lian, Z. Dai, S. Meng, and J. Ni, *Phys. Rev. B* **98**, 134514 (2018).
- [80] I. Errea, M. Calandra, and F. Mauri, *Phys. Rev. Lett.* **111**, 177002 (2013).
- [81] M. Lüders, M. A. L. Marques, N. N. Lathiotakis, A. Floris, G. Profeta, L. Fast, A. Continenza, S. Massidda, and E. K. U. Gross, *Phys. Rev. B* **72**, 024545 (2005).
- [82] G. Marini, P. Barone, A. Sanna, C. Tresca, L. Benfatto, and G. Profeta, *Phys. Rev. Materials* **3**, 114803 (2019).
- [83] B. T. Matthias, The Empirical approach to Superconductivity, in *Advances in Cryogenic Engineering*, edited by K. D. Timmerhaus (Springer, Boston, MA, 1995), Vol. 13, pp. 1–8.
- [84] J. Wang, X. Song, X. Shao, B. Gao, Q. Li, and Y. Ma, *J. Phys. Chem. C* **122**, 27820 (2018).